# Mapping the Thermal Structure of Southern Africa From Curie Depth Estimates Based on Wavelet Analysis of Magnetic Data With Uncertainties

**M. Sobh[1,2]** , **C. Gerhards[1]** , **I. Fadel[3]** , **and H.-J. Götze[4]**

[1]Institute of Geophysics and Geoinformatics, TU Bergakademie Freiberg, Freiberg, Germany, [2]National Research Institute of Astronomy and Geophysics (NRIAG), Cairo, Egypt, [3]Faculty of Geo-Information Science and Earth Observation, University of Twente, Enschede, The Netherlands, [4]Institute of Geoscience, Christian-Albrechts-University Kiel, Kiel, Germany

**Abstract** Surface heat flow provides essential information on the thermal state and thickness of the lithosphere. Southern Africa is a mosaic of the best-preserved and exposed crustal blocks, assembled in the early late Archean and then modified by a series of major tectono-thermal events, both of Precambrian and Phanerozoic. Understanding the thermal and compositional structure of the southern African lithosphere provides crucial information for the actual causes, processes of lithospheric stability, and modification. Curie depth, interpreted as the depth to 580°C, provides a valuable constraint on the thermal structure of the lithosphere. Due to the sparse distribution of surface heat flow data, we examine the degree to which the thermal structure of the crust can be constrained from Curie depth estimates in southern Africa. We provide a Curie depth map for southern Africa (obtained from the inversion of magnetic anomaly data via power spectral methods and wavelet analysis) alongside with a heat flow map (based on the previous Curie depth estimates), both equipped with uncertainties via a Bayesian approach. Opposed to other cratonic regions, the observation of a shallow Curie depths and low heat flow over the Kaapvaal Craton suggests a thermochemical reworking of the cratonic lithosphere in this region. Furthermore, a comparison with a model for the Moho depth reveals significant variations of the Curie depth, which may be located below or above the Moho in large regions. Both observations indicate that in certain regions magnetic anomaly based Curie depth estimates may reflect a compositional rather than a temperature controlled constraint.

**Plain Language Summary** The thermal state and thickness of the lithosphere are reflected, among other quantities, in the surface heat flow. While heat flow data are rather sparse, magnetic anomaly maps are widely available and allow, under certain conditions, the estimation of the bottom of the magnetized layer within the lithosphere. Latter can be associated with the 580°C-isotherm (frequently called the Curie depth), therefore allowing inferences on the thermal state of the lithosphere from magnetic data. Here, we use classical power spectral methods in combination with wavelet analysis and Bayesian methods to estimate the Curie depth and its uncertainty from magnetic anomaly maps, and subsequently, use it to estimate the surface heat flow over southern Africa. Comparison with the sparsely available measured heat flow allows us to assess the quality of the estimation and to interpret it with respect to the lithospheric structure. Southern Africa is particularly suitable for such a study due to its well-preserved and well-studied crustal blocks. The shallow Curie depths and low heat flow observed over the Kaapvaal Craton suggest a thermal reworking of the old lithospheric structures in this region. Comparison with a Moho depth model further suggests that in some regions the obtained Curie depth estimates do not necessarily reflect a temperature controlled but rather a compositional boundary.

## 1. Introduction

Estimating the spatial variations in the temperature within the Earth is important to constrain the thermal structure and the rheology of the lithosphere (Audet & Gosselin, 2019). Curie depth estimates, which correspond to the depth where crustal rocks reach their Curie temperature (∼580°C for magnetite; Dunlop & Özdemir, 2001) give independent temperature constraints over an area where magnetic anomaly data are available. Above the Curie temperature, the ability of rocks to preserve ferromagnetic magnetism

deteriorates (Haggerty, 1978) and those rocks become paramagnetic. Therefore, we identify the Curie depth with the depth of the magnetized crust.

This offers crustal temperature information at depths that boreholes cannot reach (Andrés et al., 2018) and, consequently, yields a valuable constraint for geothermal heat flow (Kaban et al., 2014). In this paper, we use a classical power spectrum inversion method (Bouligand et al., 2009; Maus et al., 1997) to obtain Curie depth estimates from magnetic anomaly data over southern Africa. This region is an ideal location for a Curie depth study due to its well preserved and well studied geology and the wide availability of geophysical data. Curie depth estimation from the power spectrum is traditionally performed using a windowed Fourier transform approach (e.g., Bouligand et al., 2009; Li et al., 2017) which is known to cause estimation problems (e.g., Audet & Gosselin, 2019). Here we combine the inverse spectral method with a 2-D wavelet approach (Gaudreau et al., 2019; Kirby, 2005) and a Bayesian framework (Audet & Gosselin, 2019; Mather & Delhaye, 2019; Mather & Fullea, 2019) to alleviate some of those problems and to provide uncertainties for the obtained Curie depths.

Despite the importance of Curie depth estimation from magnetic data, the question arises whether the spectral techniques can provide reliable depth estimates and if these estimates represent the Curie isotherms or a structural boundary (Ebbing et al., 2009). This can be a concern particularly in the stable cratonic lithosphere and when the tectonic domain is overprinted by thermal events (e.g., magmatic intrusions). In order to shed some more light on this, we use the obtained Curie depth model from Section 4.1 as prior information for the computation of the surface heat flow across southern Africa. We use two different setups to do so: (a) assuming laterally uniform thermal conductivity and heat production and (b) allowing laterally varying thermal conductivity and heat production. Deriving heat flow from such indirect information is important due to only sparsely available direct heat flow measurements (Li et al., 2017). It can be used to constrain other models of thermally controlled properties and processes (Gard & Hasterok, 2021). The obtained surface heat flow models are subsequently compared to the available direct heat flow measurements over southern Africa.

Apart from providing the Curie depth and heat flow models for southern Africa, together with uncertainty estimates, we interpret them in a geological context to judge the overall suitability of magnetic anomaly based Curie depth estimates and to identify geological conditions in which such estimates can be reliable. The used data and the obtained models are described in Sections 3 and 4, respectively. The discussion and interpretation in the context of the region's geology and tectonics as well as the comparison of our Curie depth model with an existing Moho model is provided in Section 5.

## 1.1. The Tectonic Settings of Southern Africa

The tectonics of southern Africa are described by diverse terrains that consist mainly of Archean cratonic blocks, mobile belts, and sedimentary basins (cf. White-Gaynor et al., 2020 and Figure 1). The Archean Cratons represent the ancient and stable core of the shield. The Cratons are surrounded by mobile belts that were under phases of rifting and accretion during the different orogenic cycles in the Archean and Proterozoic; this continued during the Phanerozoic. Within the Craton and the mobile belts, Precambrian terrains exit, which have experienced Phanerozoic compressional tectonics, flood basalt volcanism, rifting, and plateau uplifting. On top of these diverse tectonic units, there exist several sedimentary basins developed during the Neoproterozoic and early Palaeozoic times with depths that currently reach up to 15 km (e.g., Fadel et al., 2018).

Southern Africa has three main Cratonic blocks that form the Archean nuclei, the Kaapvaal, Zimbabwe, and Congo cratons. The oldest rock records in Kaapvaal and Zimbabwe Cratons belong to Neoarchean (de Wit et al., 1992). Suturing the two cratons in the Limpopo Belt which formed during the Neoarchean collision between the two cratons. The three units together form the greater Kalahari Craton (de Wit et al., 1992). Several tectono-thermal events affected the Kalahari Craton, including rifting and orogenic events, where the last recorded ones are: (a) The Great Karoo Dikes emplacement in the Zimbabwe craton in the late Neoarchean (c. 2.6 Ga; Jelsma & Dirks, 2002), and (b) the formation of the largest igneous intrusive body in the Earth, the Bushveld igneous complex, during the Paleoproterozoic (c. 2.1 Ga) within the Kaapvaal craton (Figure 1; Olsson et al., 2010). To the northwest of the study area is the Congo Craton consisting of
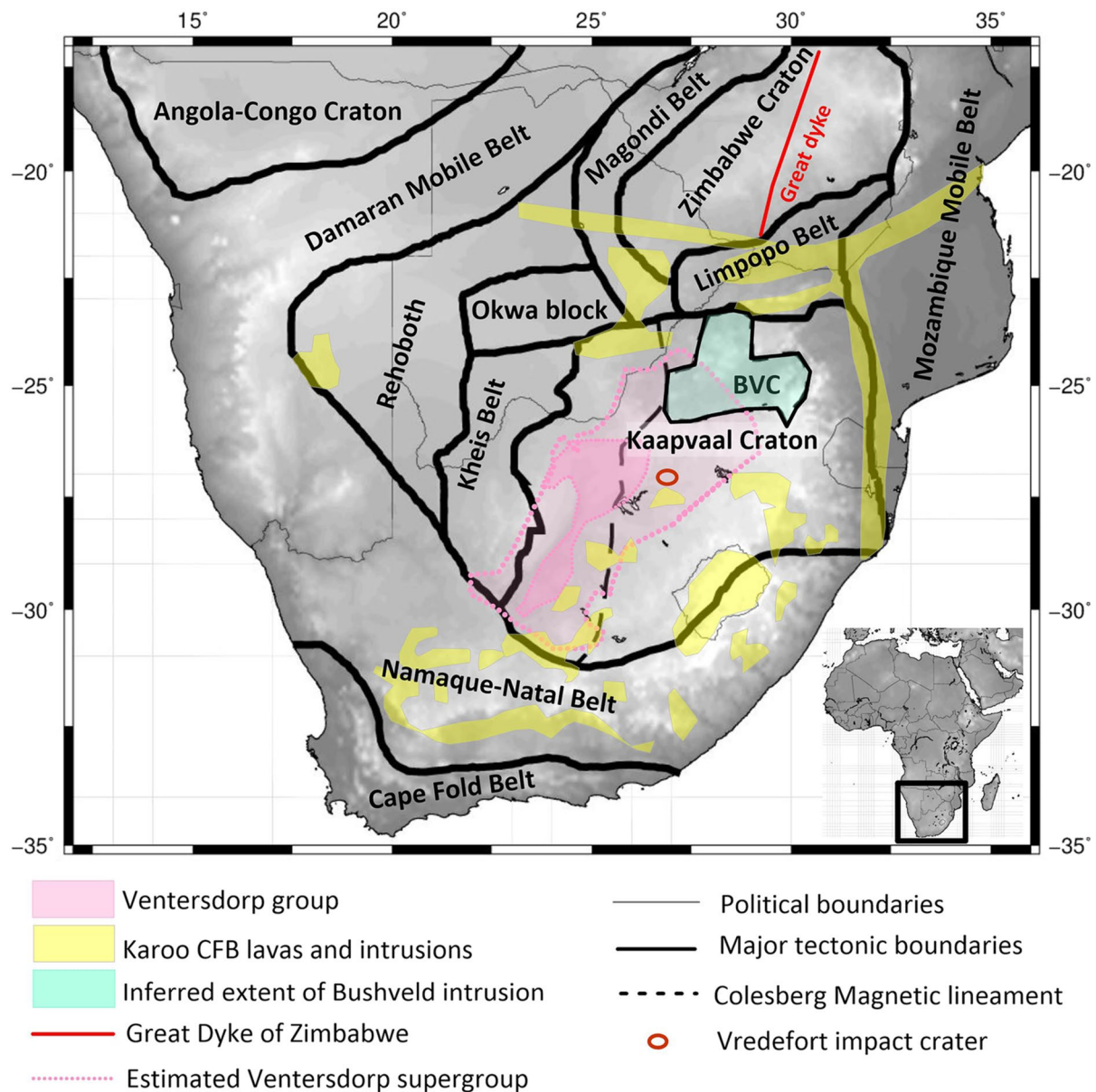
**Figure 1.** Simplified tectonic map of Southern Africa overlain with the gray shaded topography, based on ETOPO1 (Amante & Eakins, 2009). BVC = Bushveld Igneous Complex. Tectonic boundaries (de Wit et al., 1992; Goodwin, 1996); the Neoarchean Ventersdorp magmatic province (Schmitz & Bowring, 2003), the inferred extent of the Bushveld Igneous Complex (Campbell et al., 1983), and of the Umkondo continental flood basalt province (R. E. Hanson et al., 2004); major Karoo lavas and outcrops (Riley et al., 2006).

Archean and Paleoproterozoic rock units (Begg et al., 2009; Ernst et al., 2013). The Rehoboth Province has an Archean nucleus and is considered one of the poorest-defined regions in the study area (Van Schijndel et al., 2011).

The southern Africa Archean terranes are surrounded by mobile belts which formed by the accretion and reworking of the boundaries of the Archean unit during the Proterozoic (Figure 1). The Rehoboth Province and the Kheis Belt accreted during the Paleoproterozoic at the Kaapvaal Craton western edge (R. Hanson, 2003). Following this, the Namaqua-Natal Mobile Belt formed and surrounded the southern margins of the Rehoboth province and Kaapvaal Craton in the Mesoproterozoic (c. 1.2–1.0 Ga; McCourt et al., 2001). The Magondi-Okwa-Kheis belts, located in the northwest and the center of the study area, formed during

the Paleoproterozoic (c. 2.0–1.8) and accreted due to the Eburnean Orogeny to the northwestern border of the Kalahari Craton (Begg et al., 2009).

Two major Pan-African orogenic belts exist within the study area, the Mozambique Belt and the Damara Ghanzi-Chobe Belt (hence called Damaran Mobile Belt). The Mozambique Belt originated in the eastern part of the study region during the final stage of the Gondwana assembly in the Neoproterozoic (c. 841–632 Ma; R. Hanson, 2003). The Damaran mobile Belt formed during the collision between the Congo and the Kalahari cratons between the two cratonic blocks in the late Neoproterozoic to the Cambrian (c. 580–500 Ma). The original breakup of Gondwana corresponded with the creation of the c. 180 Ma Karoo major igneous province and the rifting of the Karoo over southern Africa (Duncan et al., 1997). The Cenozoic era is characterized by the emergence of the initial rifts caused by the spread of the EARS to the South. Seismically active fault systems indicate that rifting is developing in the Okavango Rift Zone (ORZ) in northern Botswana (Schmitz & Bowring, 2003), with the EARS potentially extending to central Botswana as well (Fadel et al., 2020). The different tectonic domains with different tectonic history and different ages (varying from old Cratonic lithosphere, mobile belts, and Phanerozoic rifting to flood basalt volcanism combined with the plateau uplift and the terminus of the EARS) make southern Africa an open laboratory to study and map the variations of Curie depth along with different domains which have different tectonic history and current thermal states.

## 2. Methodology

There are two steps applied in the proposed workflow: First, the Curie depth is estimated from magnetic anomaly data (described in Section 2.1) and, subsequently, geothermal heat flow is estimated based on Curie depth constraints (described in Section 2.2).

### 2.1. Curie Depth Estimation

Various spectral methods have been proposed and applied to estimate depth to the bottom of the magnetized layer in the lithosphere (e.g., Tanaka et al., 1999; Audet & Gosselin, 2019; Bouligand et al., 2009; Chopping & Kennett, 2013; Gaudreau et al., 2019; Li et al., 2017; Maus et al., 1997; Salem et al., 2014). This depth will be identified with the Curie depth throughout the remainder of this paper. We refer to the recent overviews by Núñez et al. (2021); Audet and Gosselin (2019) for a comparison of some of the approaches. In the following, we briefly describe the specific setup used in our approach.

We assume that the magnetized layer of the lithosphere is confined between two surfaces at depths $z_t$ (top of the magnetized layer) and $z_b$ (bottom of the magnetized layer). We note that $z_t = 0$ would indicate that the top of the magnetized layer coincides with the plane where data are measured. The thickness of the magnetized layer is denoted by $\Delta z = z_b - z_t$. Within this layer, we assume the magnetization to be of self-similar nature, described by a power-law $\beta$ reflecting the 2-D fractal dimension. This yields an expression for the power spectrum $\Phi_M$ of the underlying magnetization of the form

$$\Phi_M(k) = Ck^{-\beta}, \tag{1}$$

where $k = |\mathbf{k}|$ and $\mathbf{k} = (k_x, k_y)$ is the wavenumber in the horizontal plane; $C$ is some proportionality constant. Given these assumptions, the radial power spectrum $\Phi$ of the magnetic anomaly corresponding to the previously described magnetization can be expressed by (e.g., Audet & Gosselin, 2019)

$$\ln(\Phi(k)) = A - 2kz_t - \beta\ln(k) + 2\ln(1 - e^{-k\Delta z}), \tag{2}$$

where $A$ collects all constant terms.

#### 2.1.1. Wavelet Transform

The computation of the radial power spectrum is typically done using a windowed Fourier transform, where an adequately sized square window is moved across the study region. Such windowing procedures may lead to "spectral leakage" that particularly affects the low wavenumbers of the power spectrum. This has been acknowledged, for example, in Bouligand et al. (2009) by including various window sizes and has

been further studied in Audet and Gosselin (2019). In order to reduce such effects, we use a continuous wavelet transform approach as implemented in Gaudreau et al. (2019). In this approach, the wavelet transform of the magnetic anomaly map $f$ is computed at varying scales $a$ (decreasing $a$ indicate an increasing spatial localization of the wavelet $\psi_{a,\mathbf{b}}$).

$$W_{a,\mathbf{b}}[f] = \int_{\mathbb{R}^2} f(\mathbf{r}) \psi_{a,\mathbf{b}}(\mathbf{r}) \, d\mathbf{r} \tag{3}$$

This does not require explicit windowing and all available data can be used for the computation of $W_{a,\mathbf{b}}[f]$. The parameter $\mathbf{b}$ denotes the spatial shift of the wavelet and corresponds to the locations at which we want to evaluate our procedure. A wavenumber $k$ can be related to a corresponding scale parameter $a$, which enables the use of the wavelet scalogram $S(a, \mathbf{b}) = |W_{a,\mathbf{b}}[f]|^2$ for the estimation of the radial power spectrum $\Phi(k)$. The scalogram provides a local estimate of the radial power spectrum, and the theoretical expression (2) can, in turn, be used to invert for the parameters $A$, $z_t$, $\beta$, and $\Delta z$ in the vicinity of the location $\mathbf{b}$. Using such a wavelet setup can ameliorate issues with the estimation of low wavenumber contributions as they appear when applying classical windowing procedures. However, not every choice of wavelet $\psi_{a,\mathbf{b}}$ is equally well-suited for the reproduction of a Fourier power spectrum. Kirby (2005) has shown that Morlet fan wavelets $\psi_{a,\mathbf{b}}^\theta$ with azimuth $\theta$ best reproduces the properties of the Fourier spectrum. Their use requires a slight modification of the wavelet scalogram, reflecting the average of the squared wavelet coefficients over a range of $N_\theta$ varying azimuths $\theta_i$:

$$S(a, \mathbf{b}) = \frac{1}{N_\theta} \sum_{i=1}^{N_\theta} |W_{a,\mathbf{b},\theta_i}[f]|^2 . \tag{4}$$

For more details, the reader is referred to Gaudreau et al. (2019); Audet and Gosselin (2019), whose corresponding code we will use for our later computations.

### 2.1.2. Bayesian Setup

In what follows, we describe the Bayesian framework that we use to obtain information on $A$, $z_t$, $\beta$, and $z_b$ (note that $z_b$ is easily related to $\Delta z = z_b - z_t$ which appears in the theoretical power spectrum (Equation 2)). We are interested in posterior distribution $P(\mathbf{m}|\mathbf{d})$ of the parameters $\mathbf{m} = (A, z_t, \beta, z_b)$, provided some input data $\mathbf{d}$ (in our case, this will be the radial power spectrum $\mathbf{d} = (\Phi(k_1), ..., \Phi(k_n))$ at various wave numbers $k_1, ... k_n$; obtained via wavelet transforms of a magnetic anomaly map as described in the previous subsection). Our later illustrations on the obtained Curie depth $z_b$ (cf. Figure 5) represent the mean of this posterior distribution, while the uncertainty is expressed in terms of the standard deviation of the posterior.

The classical Bayes formula for the posterior reads as follows:

$$P(\mathbf{m}|\mathbf{d}) \propto P(\mathbf{d}|\mathbf{m}) \, P(\mathbf{m}), \tag{5}$$

where $P(\mathbf{d}|\mathbf{m})$ denotes the likelihood and $P(\mathbf{m})$ the prior. The prior is chosen to be a uniform distribution, not preferring any particular value of the parameter set. However, for our Curie depth models we fix the depth to the top of the magnetization $z_t$ (this is done by the sediment thickness provided by CRUST1.0 (Laske et al., 2013), assuming that the magnetization of sediments is negligible; cf. Section 3.3), and we also fix the fractal parameter $\beta$ but we run the computations for various fixed $\beta$ in the range of 1.5–4.0, with grid step 0.5, values that have been considered reasonable by earlier geological studies. In other words, our prior only assumes a uniform distribution of the parameters $\mathbf{m} = (A, z_b)$. It is known that the parameters $A$, $z_t$, $\beta$, $z_b$ are strongly interrelated, e.g., an increase in $\beta$ can be compensated by a decrease in $z_b$ (cf. Audet & Gosselin, 2019; Bouligand et al., 2009; Gaudreau et al., 2019 for a study on this). Thus, fixing $z_t$ and $\beta$ introduces some bias, but we alleviate this by testing with various fixed $\beta$, as indicated above. Furthermore, in Section 4.1.1, we briefly illustrate the influence of considering $\beta$ as an additional free parameter in the Bayesian setup. The likelihood is assumed to be a Gaussian distribution whose mean value $\boldsymbol{\mu}_{\mathbf{m}}$ is provided by the theoretical power spectrum (Equation 2) and whose variance $\sigma_{\mathbf{d}}^2$ is computed from the input magnetic anomaly map. This leads to the following expression of the posterior distribution:

$$P(\mathbf{m}|\mathbf{d}) = C \exp\left( -\sum_{i=1}^{n} \frac{|\mu_{\mathbf{m}}^i - d_i|^2}{2|\sigma_{\mathbf{d}}^i|^2} \right), \tag{6}$$

for some constant $C$. This distribution is then sampled via a Metropolis-Hasting algorithm in order to obtain the posterior mean and variance of the parameters $\mathbf{m}$, in particular of $z_b$. For some more details, we refer the reader to Audet and Gosselin (2019); Mather and Fullea (2019); Mather and Delhaye (2019). In particular, we will be using the code of Audet (2020) for our later computations.

To conclude this section, we note that these methods have some further inherent shortcomings that cannot be easily addressed. One issue is the necessity of $z_t$ and $z_b$ being constant in order to derive the theoretical power spectrum (Equation 2) and the contradiction of the assumption of a self-similar magnetization to an expression via Fourier integrals (although the latter can be ameliorated by conceiving it in terms of "bandlimited self-similarity"; Maus et al., 1997). Alternative approaches to Curie depth estimation via spectral methods are currently under development (Ebbing et al., 2021) but are not addressed here.

### 2.2. Geothermal Heat Flow

We consider two setups for the heat flow modeling, one using laterally constant conductivities and another one allowing laterally varying conductivities.

#### 2.2.1. Laterally Constant Thermal Conductivities

To determine the heat flow distribution, we assume steady-state conditions with no lateral variation in material properties and heat production (e.g., Afonso et al., 2019). Then, Fourier's Law states:

$$K_1 \frac{\partial T(z)}{\partial z} = -q(z), \tag{7}$$

$T$ stands for the temperature, $z$ stands for the depth, while $q(z)$ and $K_1$ denotes the heat flux and thermal conductivity, respectively. If initial conditions are provided by knowledge of $z_b$ as the Curie depth, $T_c$ as the Curie temperature ($\sim 580°C$) and $T_0$ as the surface temperature, then the aforementioned differential equation solution results in the following surface heat flow (e.g., Martos et al., 2017):

$$q_s = \frac{K_1(T_c - T_0)}{z_b} + H_0 h_r - \frac{H_0 h_r^2}{z_b}\left(1 - e^{\frac{-z_b}{h_r}}\right), \tag{8}$$

where $H_0$ is the radiogenic heat production, and $h_r$ stands for scale depth where $H_0$ decreased to $1/e$ from surface value; assuming an exponential decrease of heat production with depth (e.g., Lachenbruch, 1970).

Later on, we refer to this setup as the 1-D model or "constant conductivity model" because we assume $K_1$ to be constant within the entire crust and mantle. The corresponding surface heat flow models indicated in Sections 4.2 and 5.2 are computed from Equation 8, using the Curie depth $z_b$ obtained in Section 4.1 and fixing $H_0 = 2\,\mu W/m^3$, $h_r = 10$. The outcome is typically indicated for various (but fixed) thermal conductivities $K_1$. Furthermore, we provide some basic indicators of uncertainty for the heat flow: we compute $q_s$ based on $z_b$ as well as on $z_b \pm \sigma$ (where $\sigma$ denotes the uncertainty of $z_b$ as indicated in the results in Section 4.1) and provide the maximum of the residuals between the three resulting outcomes as a measure of uncertainty for the surface heat flow $q_s$.

#### 2.2.2. Varying Thermal Conductivities

We allow different thermal conductivities $K_1$ and $K_2$ within the crust and the mantle, respectively. Furthermore, the heat flux is assumed to be purely vertical and each lithospheric column is in thermal equilibrium. Thus, within each column, $K_1$ and $K_2$ are constant, but the thermal conductivities are allowed to vary (laterally) among the different columns.

Given this setup, Fourier's law (Equation 7) can be used to derive the temperature dependence with respect to depth, analogously to the 1-D case indicated above. Following Lösing et al., 2020, we separate the temperature distribution into two regimes: within the lithospheric mantle, that is, a depths $z > M$ (where $M$ denotes the depths to the Moho), where we assume that no heat is produced (Afonso et al., 2013). Thus, the

temperature increases linearly with depth. Within the crust, that is, at depths $z \leq M$, we assume that the heat production decays exponentially. This leads to the following temperature distribution:

$$T(z) = T(M) + \frac{q_D}{K_2}(z - M), \qquad z > M, \tag{9}$$

$$T(z) = T(0) + \frac{(q_D + H(M))z - \bar{H}(z)}{K_1}, \qquad z \leq M. \tag{10}$$

By $q_D$ we denote the heat flux at the Moho. Furthermore, $\bar{H}(z) = \int_0^z H(s)ds$, where $H(z) = H_0 \exp(-z/h_r)$ denotes the exponentially decaying heat production rate in the crust (Martos et al., 2017). The temperature at the Moho $T(M)$, as required in Equation 9, is defined via $T(M) = T(0) + ((q_D + H(M))M - \bar{H}(M))/K_1$, using Equation 10. The heat flux $q(z)$ at any specific depth $z$ within the crust is a result of the total heat production subtracted from the surface heat flux $q_s$, so we obtain the following simple relation between the surface heat flux $q_s$ and the heat flux $q_D$ at the Moho:

$$q_s = q_D + H(M). \tag{11}$$

with the above in mind, one can see that Equation 10 is essentially a rearranged version of Equation 8. However, since we now have the Moho depth as a boundary between two regimes and since we have more unknowns than in the case of constant thermal conductivity, we cannot simply evaluate (Equation 10), resp. (Equation 8), anymore to obtain $q_s$.

Assuming knowledge of the Curie depth $z_b$ (which is obtained from our results in Section 4.1), the Moho depth $M$ and the depth to the Lithosphere-Asthenosphere boundary $z_{LAB}$ (both extracted from the models described in Section 3.4), Equations 9 and 10 can be used to constrain the parameters $q_D$, $H_0$, $K_1$, $K_2$ via

$$T(0) = T_0, \quad T(z_b) = T_c, \quad T(z_{LAB}) = T_{LAB}. \tag{12}$$

The Moho depth influences these equation indirectly through its involvement in Equations 9 and 10. The input temperatures are set to the values $T_0 = 0°C$ (temperature at the surface), $T_c = 580°C$ (temperature at the Curie isotherm), $T_{LAB} = 1,315°C$ (temperature at the Lithosphere-Asthenosphere Boundary), as is also done in related works.

A Bayesian framework similar to that in Section 2.1.2 can be used to obtain the parameters $\mathbf{m} = (q_D, H_0, K_1, K_2)$ within each lithospheric column from the input $\mathbf{d} = (T_0, T_c, T_{LAB})$. Equations 9, 10, and 12 provide the required forward operator between $\mathbf{m}$ and $\mathbf{d}$. In contrast to the setup of the 1-D model from before, the thermal conductivities $K_1$, $K_2$ are not fixed anymore but will be inverted for jointly with the heat flux $q_D$ at the Moho and the radiogenic heat production $H_0$. For more details, we refer the reader to Lösing et al. (2020). The main quantity of interest to us is the posterior mean of $q_D$ that allows to obtain the desired surface heat flow $q_s$ via (Equation 11). The uncertainties available for $z_b$ are used in an identical way as in the 1-D model setup to provide basic indicators of uncertainty for the surface heat flow $q_s$. The results are illustrated in Section 5.2 and we refer to this setup as "varying conductivity model."

## 3. Data

In the following section, we describe the used datasets together with any necessary initial data preparation (see Table 1 for the data sources). All data is restricted to the continental area.

### 3.1. Magnetic Data

We used the magnetic data from the recently released World Digital Magnetic Anomaly Map 2.0–WDMAM 2.0 (Catalán et al., 2016; Lesur et al., 2016). WDMAM 2.0 (www.wdmam.org) provides a 4 km grid resolution of magnetic anomalies, jointly compiled from marine cruises and airborne surveys. All data are upward-continued to 5 km height with respect to the WGS84 datum.

**Table 1**
*Summary of Used Data Sets*

| Data | Reference |
| --- | --- |
| Geophysical | |
| Magnetic data | WDMAM2 (Lesur et al., 2016) |
| Heat flow | NGHF (Lucazeau, 2019; Pollack et al., 1993) |
| Geometrical | |
| Depth to basement | CRUST1.0 model (Laske et al., 2013) |
| Depth to Moho | Gravity inversion (Uieda & Barbosa, 2017) with seismic constraints (Fadel et al., 2020; Youssof et al., 2013) |
| Depth of lithosphere | LithoRef18 (Afonso et al., 2019) |

The SaNaBoZi aeromagnetic grid (Figure 2), which stands for: South Africa, Namibia, Botswana, and Zimbabwe was created as a result of the African magnetic mapping project (Stettler et al., 2000). This new magnetic grid is part of the second version of the WDMAM 2.0 (Lesur et al., 2016) used in this study (Figure 2).

Here, we will briefly summarize the regional-scale magnetic features in the study area. The Namaqua-Natal domain is characterized by a remarkable continental-scale magnetic anomaly, namely, the Beattie Magnetic Anomaly (BMA; described by Scheiber-Enslin et al., 2014; Cornell et al., 2011). It extends over
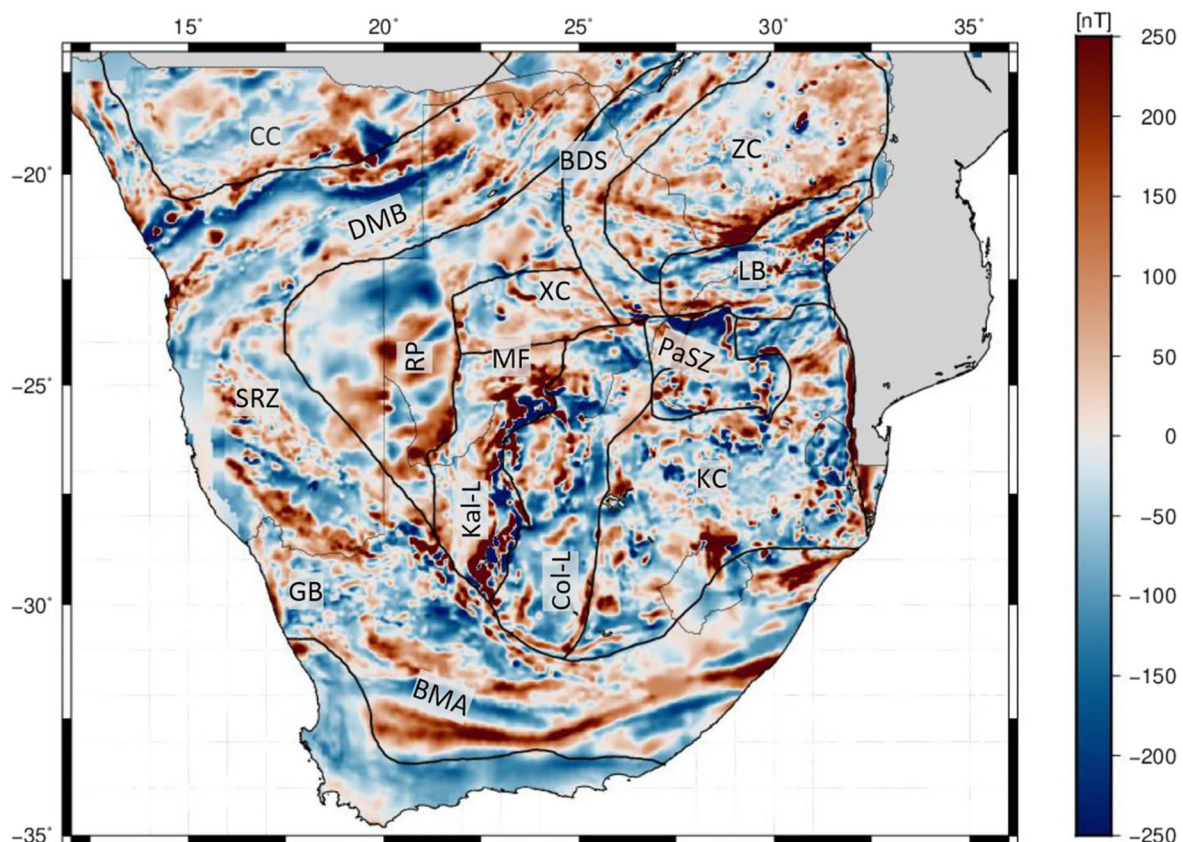


**Figure 2.** Total magnetic intensity map of southern Africa from WDMAM2.0 (Lesur et al., 2016) with 2 arc-minute grid spacing (approximately 4 km). The original data are upward-continued to 5-km altitude relative to the WGS84 datum. Black lines represent the major tectonic provinces of southern Africa (de Wit et al., 1992). BMA = Beattie Magnetic Anomaly; BDS = Botswana Dyke System; CC = Congo Craton; Col-L = Colesberg Lineament; DMB = Damaran Mobile Belt; GB = Gariep Belt; Kal-L = Kalahari magnetic lineament; KC = Kaapvaal Craton; LB = Limpopo Belt; MF = Molopo Farm; PaSZ = Palala Shear Zone; RP = Rehoboth Province; SRZ = Sinclair-Rehoboth Zone; ZC = Zimbabwe Craton.
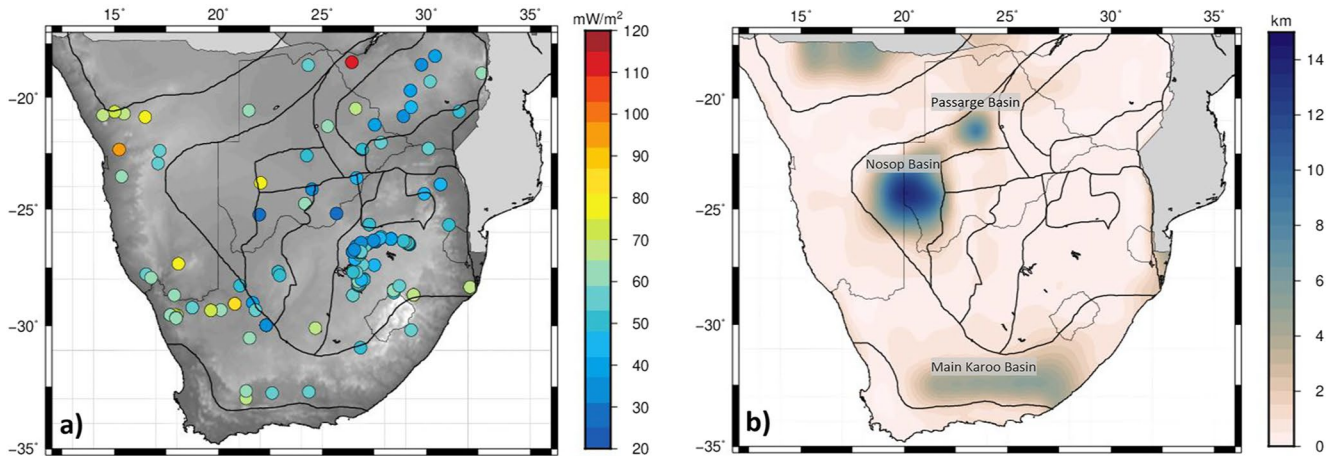
**Figure 3.** (a) Distribution of heat flow measurements within the study area from the global database (Lucazeau, 2019). The associated uncertainty of the measured heat flow values are presented in Figure S2 in the Supporting Information S1. (b) Sediment thickness map of southern Africa extract from global sediment thickness map (Laske et al., 2013) used to constrain the depth of the upper boundary of magnetized layer ($z_t$) and fixed prior to the inversion. Major sedimentary basins are presented: Main Karoo Basin (Johnson et al., 1997); Nosop Basin (Wright & Hall, 1990); Passarge Bain (Key & Ayres, 2000).

1,100 km from the western to the eastern coastal margins. To the North, the Kalahari magnetic lineament (Reeves, 1978) is characterized by short-wavelength magnetic anomaly which is interpreted as the western boundary of the Kaapvaal Craton. This anomaly is regarded as one of the most significant features of South Africa's aeromagnetic map (Cornell et al., 2011). Within the Kaapvaal Craton, the Colesberg magnetic lineament is characterized by long-wavelength magnetic anomalies. The boundary between the Kaapvaal Craton and the Limpopo Belt is characterized by a long-wavelength magnetic anomaly associated with the Palala Shear Zone (PaSZ). Moving to the North, the boundary between the Zimbabwe Craton and Limpopo Belt is relatively well defined from a clear change in the magnetic anomaly across the boundary. Moving toward the west, the magnetic anomalies along the Karoo basalts are shown in Botswana as well as the Botswana dyke swarm. In Namibia, long-wavelength, curvilinear magnetic anomalies are observed which can be associated with the Sinclair-Rehoboth Zone (Van Schijndel et al., 2011). A weak imprint of the Beattie anomaly is visible even in the global lithospheric magnetic field model from satellite (LCS-1) by Olsen et al. (2017) (see Figure S1 in the Supporting Information S1), which confirms its regional significance.

### 3.2. Heat Flow Data

The compilation of surface heat flow data used in this work (Figure 3a) comes from different sources (e.g., Pollack et al., 1993). Lucazeau (2019) updated the earlier heat flow catalogs, and compiled all available data in the New Global Heat Flow database (NGHF). Measurements are sparse and irregularly distributed and of different quality. The quality of heat flow measurements is discussed in the NGHF (Lucazeau, 2019). For each measurement, the rating group is determined by the fluctuation of the heat flow in the borehole where the measurement is done. In general, old and questionable measured values are given a lower rating. According to the NGHF database, most of heat flow data used here have an uncertainty between 10 and 20 mW/m$^2$ (Lucazeau, 2019) (see Figure S2 in the Supporting Information S1). In general, the Kaapvaal and Zimbabwe Cratons have a relatively low heat flow ($\approx$40–50 mW/m$^2$); these values increase to $\approx$60 mW/m$^2$ at the boundary between the Craton and the surrounding Proterozoic and Pan-African mobile belts. Mobile belts surrounding the Kaapvaal Craton exhibit the highest heat flow signatures in South Africa ($\approx$70 mW/m$^2$), which may be linked to underlying geological, tectonic and crustal compositional controls, particularly related to the heat production of radiogenic material.
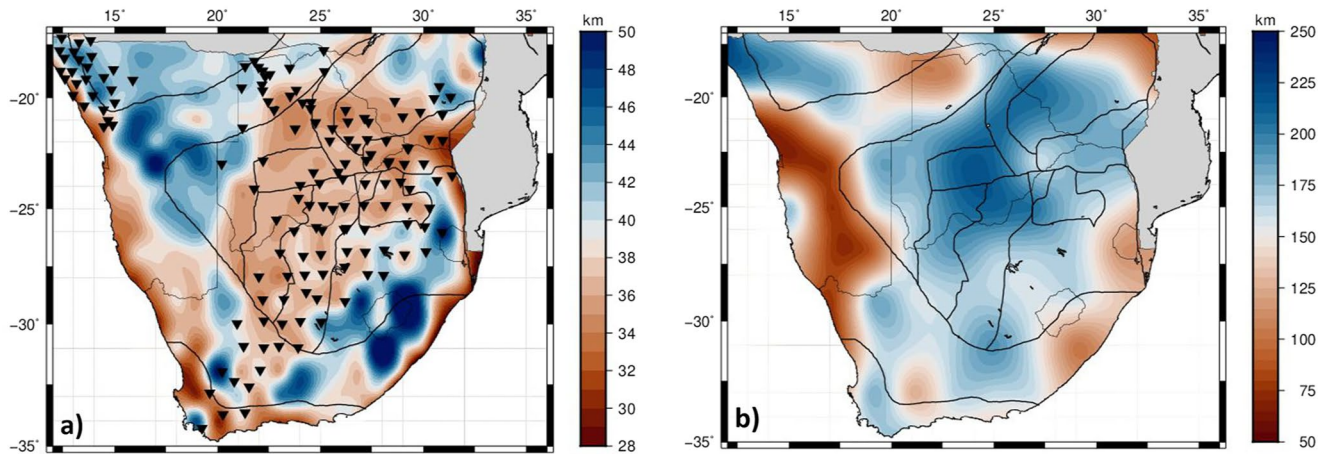
**Figure 4.** (a) Moho depth of southern Africa from seismically constrained gravity inversion; the black triangles represents the location of seismic stations used to constrain the gravity inversion for Moho depth (b) Lithosphere-Asthenosphere boundary depth derived from LithoRef18, the global reference model of the lithosphere (Afonso et al., 2019).

### 3.3. Sediment Thickness

The sediment thickness is derived from the sediment layers of CRUST1.0 model (Laske et al., 2013). The original resolution of the sediment layer is 1° × 1°, and we interpolate it to 4 km sampling interval to be compatible with the magnetic data resolution. The sediment thickness map in Figure 3b is used to constrain the depth to the top of the magnetized layer ($z_t$), assuming that the magnetization of sediments is negligible (Ellwood et al., 2000; Gaudreau et al., 2019).

### 3.4. Crustal and Lithospheric Thickness

For the purpose of comparing the Curie depth with the Moho depth in the study area and to constrain the heat flow calculations, we estimate the Moho depth by inverting satellite gravity gradients using the seismically constrained non-linear inversion scheme of Uieda and Barbosa (2017) (Figure 4a). The uncertainty of the estimated Moho depth has been discussed previously by Sobh et al. (2019, 2020) and the effects of such uncertainties on the estimated heat flow is discussed in Figure S8 in the Supporting Information S1. Since large contributions of the heat flow come from radioactive decay within an enriched crust (Hasterok & Chapman, 2011), considering the crustal thickness in our modeling process (cf. Section 2.2.2) can substantially improve heat flow maps. The lithospheric thickness model (Figure 4b) is derived from the global reference model of the lithosphere (Afonso et al., 2019).

## 4. Results

We present the obtained Curie depth and heat flow maps together with their uncertainty. Additionally, we provide an initial assessment of the variation of the involved parameters.

### 4.1. Curie Depth Estimates

The Curie depth maps, together with the estimated uncertainties, are displayed in Figure 5. As mentioned earlier, estimating all quantities $z_b$, $z_t$, and $\beta$ simultaneously may lead to ambiguous values for $z_b$ (illustrated, e.g., in Audet & Gosselin, 2019; Bouligand et al., 2009; Gaudreau et al., 2019). Therefore, following Gaudreau et al. (2019) we keep $\beta$ fixed. However, three different maps of $z_b$ are presented in Figure 5 with different (but fixed) $\beta$ values. The chosen $\beta$ values range from 2.0 to 3.0, following the typical values estimated in crustal rocks (Gaudreau et al., 2019; Maus et al., 1997). The upper boundary of the magnetized layer ($z_t$) is set to the sedimentary thickness model shown in Figure 3b. Yet, to provide at least a brief illustration
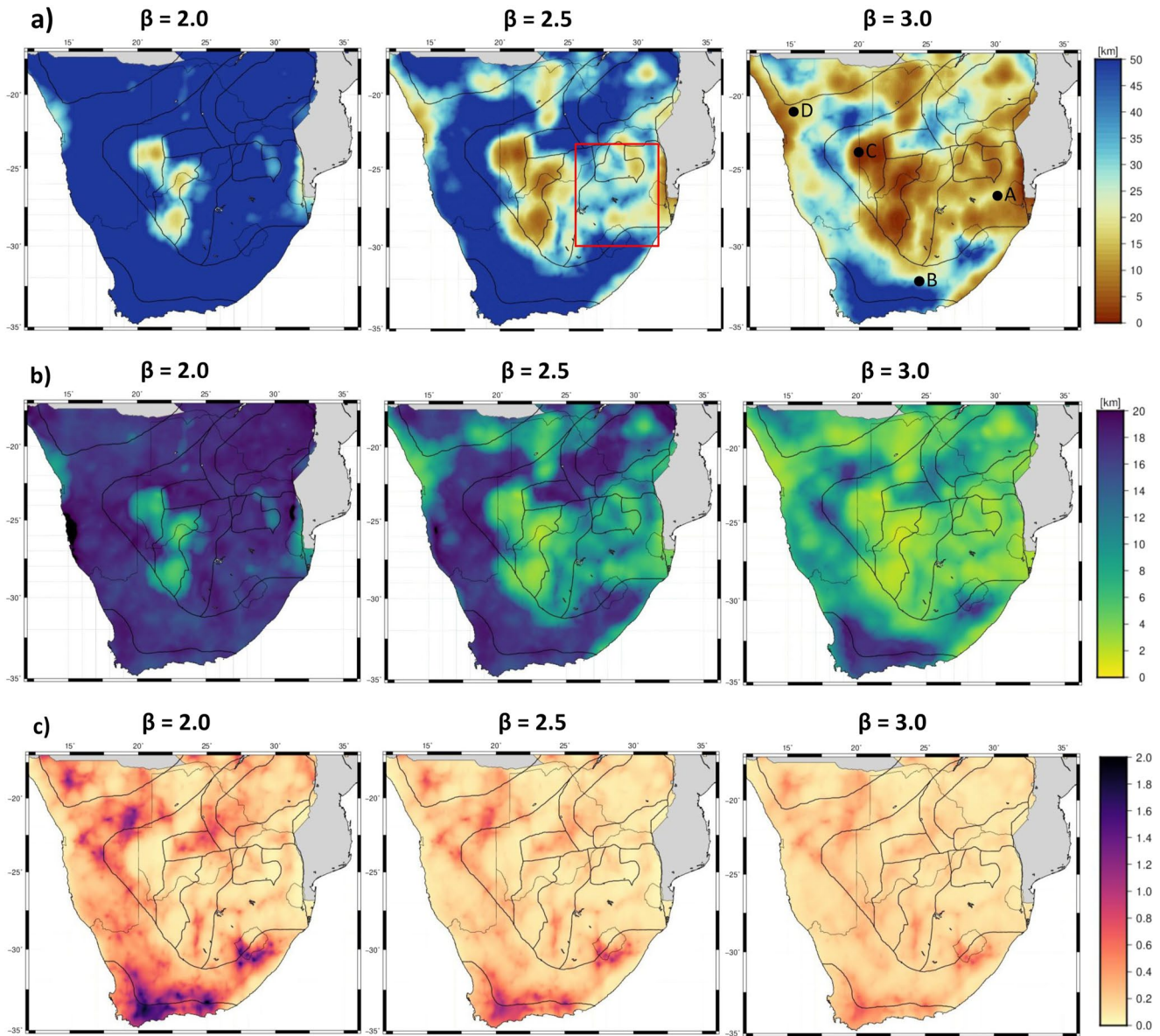
**Figure 5.** (a) Maps showing the depth to the bottom of magnetic sources ($z_b$) based on the aeromagnetic data in southern Africa when the upper boundary of magnetized layer ($z_t$) is constrained by the sediment thickness from Figure 3b and for different $\beta$ (fixed $\beta$ values are used along the whole area), demonstrating that, the $\beta$ and $z_b$ are inversely proportional. Long-wavelength features are consistent throughout all maps, regardless of $\beta$ values. The red box outlines the $z_b$ along Kaapvaal region. The locations marked by the letters A, B, C, and D correspond to the maps in Figure 6, and Figures S3–S5 in the Supporting Information S1. (b) The estimated uncertainty of the mean Curie depth in southern Africa. (c) Reduced chi-square maps.

of the influence of fixing these parameters in our setup, we use Section 4.1.1 to indicate the joint probabilities of the inversion at selected locations when inverting for all three parameters simultaneously.

Figure 5 shows the inversion results with fixed parameters as mentioned above. One can observe that an increase of $\beta$ leads to a substantial decrease of the estimated $z_b$. This has also been illustrated in the synthetic examples in Section 3.3 of Bouligand et al. (2009) and discussed also in Audet and Gosselin (2019). The estimated Curie depth $z_b$ along the Kaapvaal Craton drops from 50 to 10 km as $\beta$ increases from 2.0 to 3.0. The $z_b$ values within the Kheis Belt vary between 25 and 5 km, and along the Zimbabwe Craton, $z_b$ varies between 50 and 25 km, for $\beta$ increasing from 2.0 to 3.0. Along the northeastern margin of the Damaran Mobile Belt in northern Botswana, the mean $z_b$ ranges from 15 to 5 km, with $\beta$ increasing from 2.5 to 3.0. The mean $z_b$ along Namaqua-Natal Belt ranges from 50 to 30 km.

However, Figure 5a also indicates that the general patterns of the estimated Curie depth are robust with respect to $\beta$ (i.e., regions that reveal a shallow Curie depth compared to deeper surrounding regions remain shallow in this relative sense across the whole range of tested values of $\beta$). Therefore, these general patterns can provide some reliable geophysical information.

There are some exceptional cratonic subregions that reveal significantly shallower depth than other Archean Cratons. The northeastern margin of the Zimbabwe Craton has shallow $z_b$ values between 25 to 5 km at $\beta$ values 2.5 and 3.0, which may be related to the Great Dyke of Zimbabwe emplacement event that has most likely caused increased temperatures in the lower Crust. The eastern margin of the Kaapvaal Craton is estimated with shallow Curie depth values between 25 to 5 km along all the different $\beta$. This is probably due to the presence of Karoo lavas along the boundary between the Kaapvaal Craton and the Mozambique Mobile Belt. The western margin of the Kaapvaal Craton displays shallower Curie depth estimates, which is related to reactivation of the Kheis province during Kibaran orogeny (Thomas et al., 1993). The Kheis Belt consists of basalts and volcaniclastic sediments located between the Kaapvaal Craton to the east and the Rehoboth terrane to the west. It forms a distinct highly magnetic feature that extends northwards to the Okwa Block (Hutchins & Reeves, 1980). Toward the Cape Fold Belt, the estimated $z_b$ is very deep and appears unreasonable. This is also the area where the highest uncertainty and reduced chi-square is observed. Our Curie depth map with $\beta = 3.0$ (cf. Figure 5a) is, for the most part, consistent with the global model of Curie depth by Li et al. (2017) and follows a similar pattern of variation along the Kaapvaal Craton.

Generally, low uncertainties and chi-square values are associated with shallow Curie depths, while they significantly increase with larger Curie depths (cf. Figures 5b and 5c). According to Mather and Fullea (2019) this might be because estimating the small wave number component of the radial power spectrum is challenging. For the areas where Curie depth values are greater than 50 km, the associated uncertainty and chi-square is large for all $\beta$ values. Along the Kheis belt and Kaapvaal Craton, the chi-square values continue to be consistent across different $\beta$ values, while along the Damara Mobile Belt and Cape Fold Belt, they drop when $\beta$ increases.

### 4.1.1. Multiparameter Study for Selected Locations

In this section we briefly describe the influence of fixing the parameter $\beta$ for selected locations. Specifically, we allow all parameters $\mathbf{m} = (A, \beta, z_b)$ to vary and illustrate their marginal and joint posterior probabilities based on the methodology described in Section 2.1. The top depth $z_t$ remains fixed.

The four specific locations for this study are those that are indicated by the letters A, B, C, and D in Figure 5a (representing different tectonic domains within the study area). In each case, the first step is to estimate the three parameters $z_b$, $\beta$, and $A$ simultaneously (Figure 6a). Subsequently, $\beta$ is fixed to the mean obtained in this first step and the inversion is done only for the two remaining parameters $z_b$ and $A$ (Figure 6b).

For the grid cell (a) in the Kaapvaal Craton, the results obtained from the joint inversion of all three parameters give a $z_b$ of 26.4 km and an uncertainty of 13.2 km. The mean of $\beta$ is 3.0 with an uncertainty of 0.4. Keeping $\beta$ fixed and running the inversion again, the uncertainty of $z_b$ reduces to 10.4 km with a mean of 29.3 km, analogous to what has been obtained in Figure 5b. The result for the other three test sites (b, c, and d) are shown in Figures S3–S5 in the Supporting Information S1. The key outcome here is that the mean $\beta$ obtained during the simultaneous inversion for all three parameters $z_b$, $\beta$, and $A$ varies across all four tested tectonic domains. Nonetheless, the obtained $\beta$ for any of these domains corresponds to one of the $\beta$ for which the Curie depth has been computed and indicated over entire southern Africa in Figure 5a. This should be kept in mind when interpreting inversion results for $z_b$ with fixed $\beta$, and the appropriate map should be chosen.

### 4.2. Heat Flow Estimates

We perform a comparison between the Curie depth based heat flow model and the available heat flow measurements to validate the results of Curie depth estimation and evaluate the method to determine it from magnetic data.
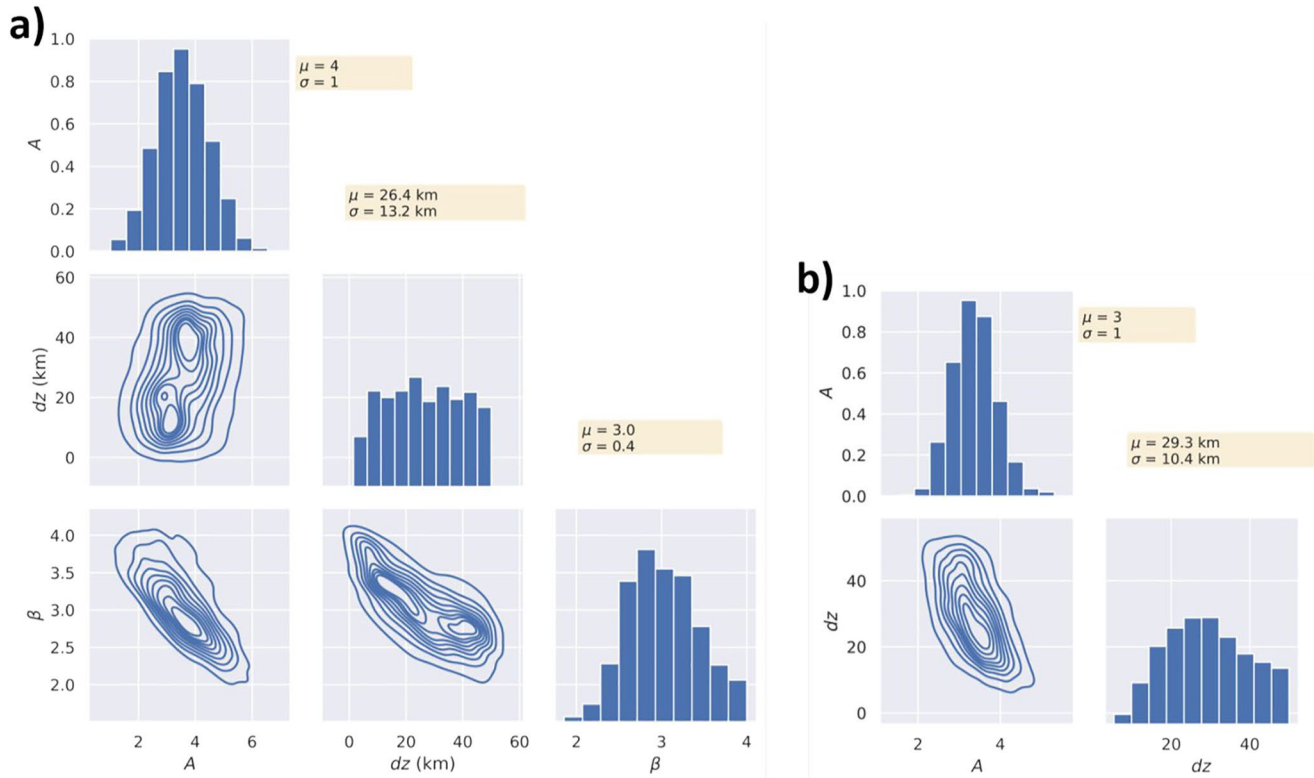
**Figure 6.** Statistical distribution of model parameters from the probabilistic Bayesian inference method at location (a) of Figure 5a: marginalized and joint posterior distribution from the simultaneous inversion for the parameters $z_b$, $\beta$, and $A$ (a) and for the simultaneous inversion for $z_b$ and $A$, with fixed $\beta = 3.0$ (b). Statistical information on each $z_b$, $\beta$, $A$ is provided in the orange boxes; $\mu$ is the mean value, $\sigma$ is the standard deviation. Note that the parameter $dz$ in the above plots indicates $\Delta z$ in our notation, so that $z_b = z_t + dz$.

Figure 3a shows the measured heat flow values along the study area. Heat flow measurements in the Kaapvaal and Zimbabwe cratons are well distributed, with values ranging from ~40 to ~60 mW/m², and along mobile belts ranging from ~55 to ~80 mW/m². On the other hand, the rest of the study area suffers from highly scattered and sparse distributions of heat flow measurements. The calculated heat flow values $q_s$ from the 1-D model in Section 2.2, based on Equation 8 with $\beta = 2.5$, are plotted versus Curie depth for different thermal conductivities $K_1$ (cf. Figure 7). We also include heat flow measurements derived from the global database Lucazeau (2019), plotted against the estimated Curie depths from Section 4.1 at the measurement locations. This comparison clearly has a considerable degree of variability. The scatter can be due to various factors: uncertainty in the assumed parameters during the Curie depth estimation, uncertainties of the heat flow measurements, and uncertainties like irregular lithological or thermal boundaries.

Unlike the first two points, the uncertainty due the lack of precise lithological boundaries cannot be quantified by any of the existing methods. This is why we discuss in Section 5 the outcome of the Curie depth estimation and the heat flow estimation jointly with the geology in southern Africa. Figure 7 shows that, in particular, the shallow Curie depth reveal a large mismatch with the measured heat flow values, implying that these shallow depths might not represent the maximum depth of the magnetic layer but correlate with the overprinted magmatic activities. Locally, however, the correlation can be quite good. Figure 8 shows an analogous scatter plot, but the $z_b$ results are restricted to the Kaapvaal Craton, since it has dense heat flow measurements for better comparison.

As shown in our previous results, larger $\beta$ than the correct value can be compensated by shallower $z_b$. Consequently, high heat flow values in our model might indicate an overestimation in comparison to the real thermal state of the study area. The heat flow results might be validated in the future by calibrating the results using some actual thermal gradient measurements.
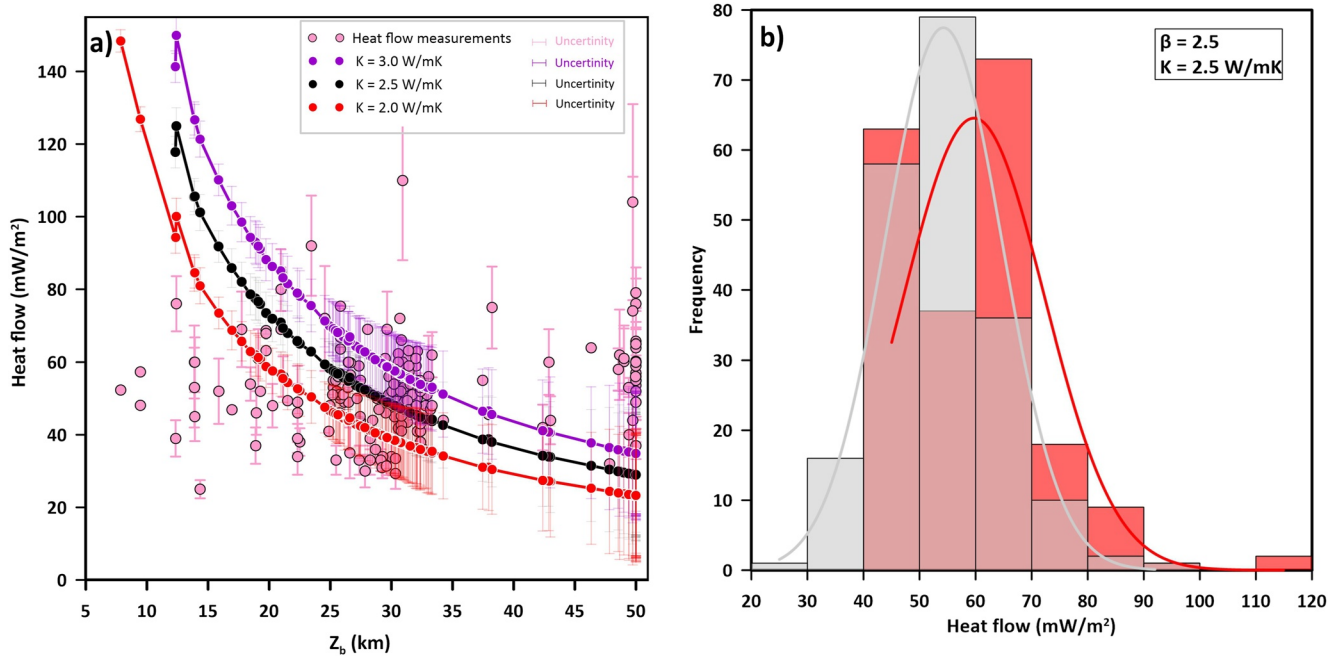
**Figure 7.** (a) Plot of the estimated Curie depth ($z_b$) against the measured and estimated heat flow (both equipped with their uncertainties). The continuous curves indicate the theoretical heat flow for different thermal conductivity 2.0 (red), 2.5 (black), 3.0 (purple). The scattered dots (light pink) represent the measured heat flow from Lucazeau (2019). (b) Frequency of estimated heat flow values (in gray) and of the measured heat flow values (in red).
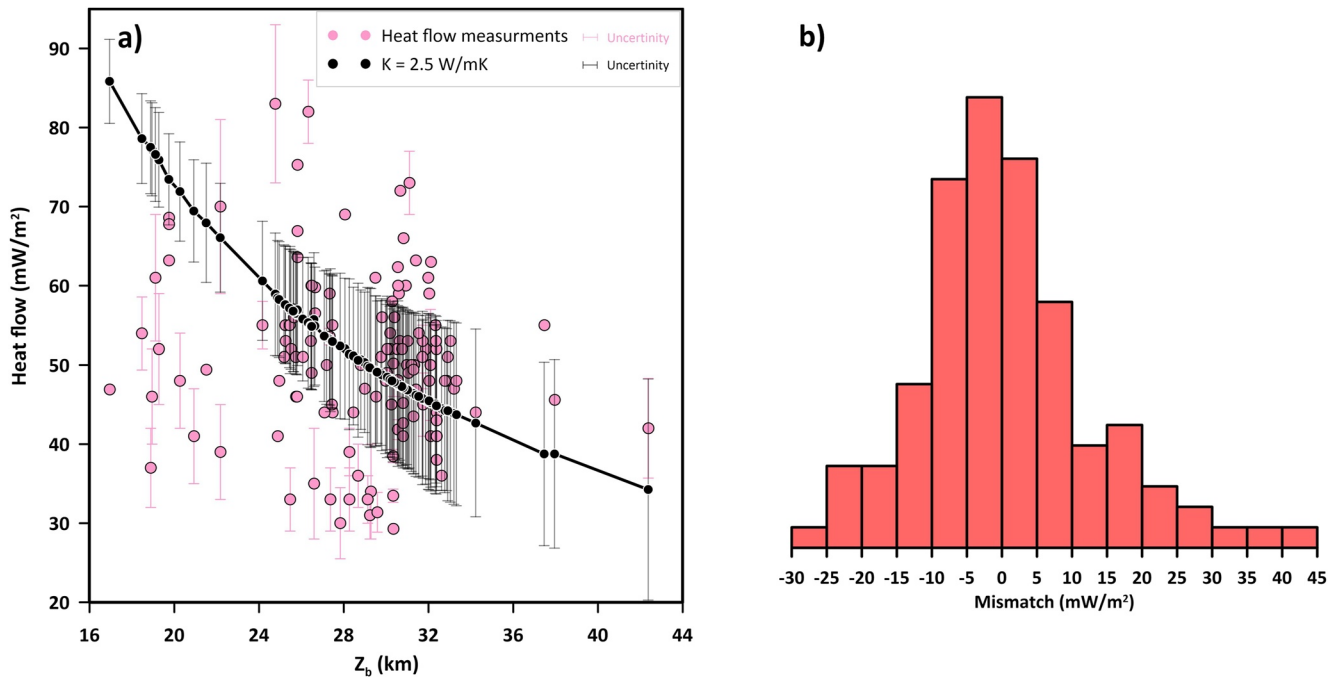


**Figure 8.** (a) Plot of the estimated Curie depth ($z_b$) against the measured and estimated heat flow (both equipped with their uncertainties). Same as in Figure 7, but restricted to the Kaavaal Craton. (b) Frequency of mismatch between the estimated and the measured heat flow.
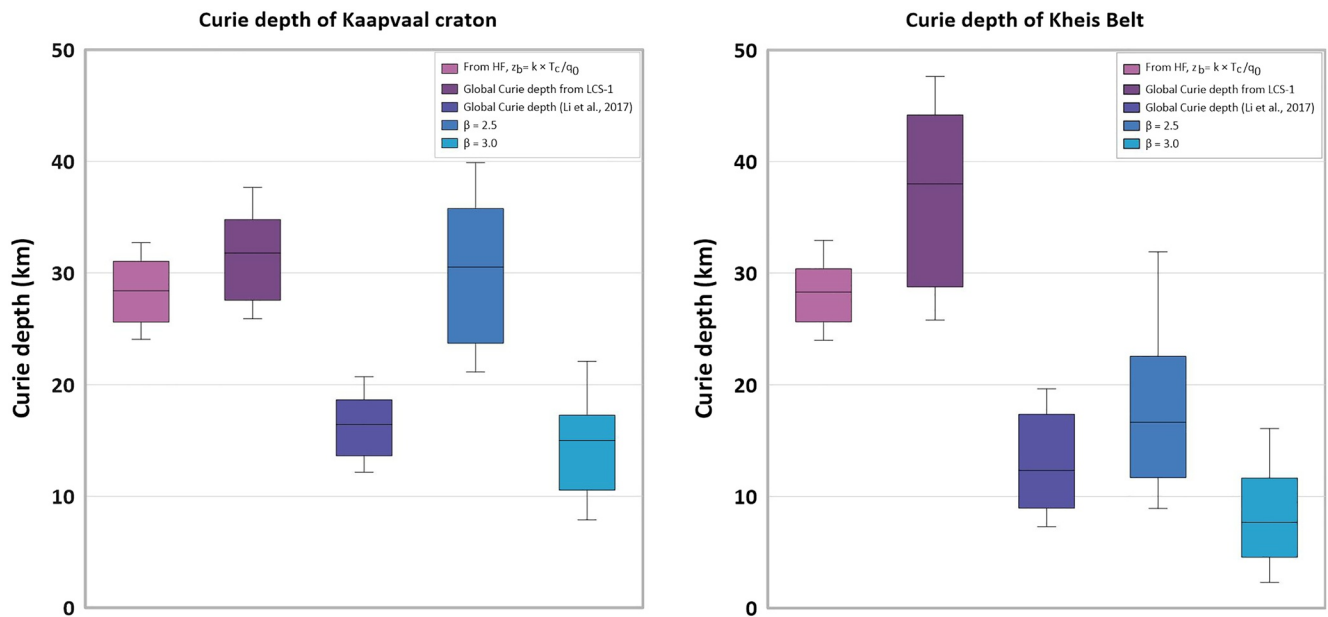
**Figure 9.** Comparison of estimated Curie depth along (a) Kaapvaal Craton; (b) Kheis belt from our model using two different $\beta$ values, from a global curie depth model by Li et al. (2017), from heat flow measurements, and from a global model of Curie depth by applying the equivalent source magnetic dipole method (Gard & Hasterok, 2021).

## 5. Discussion

### 5.1. Curie Depth Compared With Magnetic and Geological Setting

Comparing the estimated Curie depths with the magnetic data shows the following: the shallow Curie depth areas generally associated with the short-wavelength magnetic anomalies, for example, Kheis belt's magnetic signature and the Kalahari magnetic lineament (Figure 2; cf. Reeves, 1978). Deep Curie depths, on the other hand, generally correspond to areas characterized by long-wavelength anomalies, for instance, the Beattie continental scale Magnetic Anomaly (BMA; cf. Scheiber-Enslin et al., 2014; Cornell et al., 2011 and Figure S1 in the Supporting Information S1).

The first obvious observation is that the very shallow Curie depth in the middle of Botswana falls into the part of the sedimentary basins (Passarge and Nosop Basin) which are in the vicinity of the Xade complex and Okwa block intrusive bodies (cf. Figure 1). Along the Okavango Rift Zone in the north-western part of Botswana, $z_b$ is shallow ranging from 8 to 15 km, which coincides with the thermal perturbation of Okavango Rift (Leseane et al., 2015) and crustal thinning (Fadel et al., 2020). Toward the eastern part of Botswana, an intermediate Curie depth is estimated, which coincides with the Zimbabwe Craton and the old Magondi and Limpopo belts in this area.

Along the Kalahari magnetic lineament, all $\beta$ values display similar long-wavelength patterns. This suggests that these features are consistent and are geophysically significant. The anomalous shallow $z_b$ along the Kalahari magnetic lineament might be interpreted as the depth to the base of the magnetic lithology and not the Curie depth (Blakely, 1988). However, there is no recent magmatic activity recorded along this area. A more likely argument is that the Kaapvaal Craton has a distinct $\beta$ value due to a significant difference in lithology and geological history.

Recently Gard and Hasterok (2021) have determined the Curie depth globally using the satellite data based lithospheric magnetic field model LCS-1 (cf. Olsen et al., 2017), applying the equivalent source magnetic dipole method. They obtain deeper $z_b$ values along the Kheis Belt and the Kalahari magnetic lineament, due to the very long wavelengths dominating the LCS-1 magnetic data, which do not reflect the shorter wavelengths associated with the magnetic signature of the Kheis belt (cf. Figure 9b).
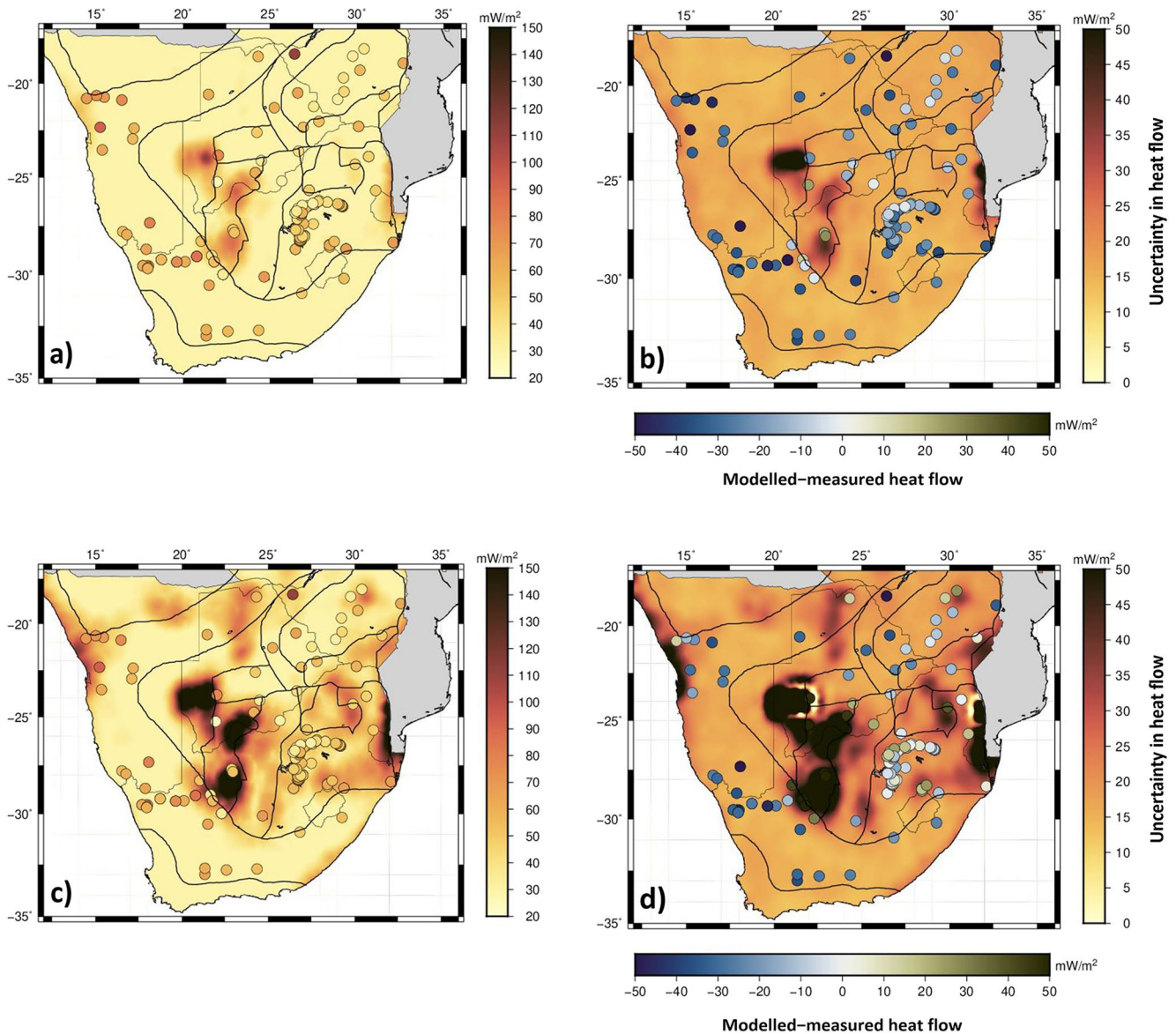
**Figure 10.** Modeled heat flow using the 1-D heat conductive model with laterally constant thermal conductivity ($k = 2.5$ W/mK) based on Curie depth estimates when (a) $\beta = 2.0$, (c) $\beta = 2.5$, overlain with the locations of measured heat flow data. Uncertainty of heat flow when (b) $\beta = 2.0$, (d) $\beta = 2.5$, overlain with the difference between modeled and measured heat flow.

The abrupt change from shallow Curie depth ($\sim 20$ km) to deep (>50 km) values coinciding with the thrust Fault between the Namaqua-Natal belt and Cape Fold Belt is the most noticeable feature in Figure 5a. Since the Namaqua-Natal belt is associated with high electrical conductivity (Weckmann et al., 2007) and low shear wave velocity (Celli et al., 2020; White-Gaynor et al., 2020), suggesting higher temperatures in the region, the estimated large Curie depth might be erroneous. In addition, at all $\beta$ values, the Cape Fold Belt shows high reduced chi-square values and high uncertainties, therefore indicating that the Curie depth in this region cannot be estimated reliably.

### 5.2. Correlation Between Curie Depth and Heat Flow Measurements

Previous studies have shown that Curie depths are inversely correlated to heat flow (Li et al., 2017). In our study, we found that measured heat flow and Curie depths estimates seem to be poorly correlated (Figure 7)

and in most cases do not match the predictions of the 1-D thermal conductivity model from Section 2.2. Locally, however, the degree of correlation improves (e.g., for the Kapvaal Craton as indicated in Figure 8).

In the following two subsections, we discuss the 1-D model as well as the model with varying thermal conductivities in more detail.

### 5.2.1. Modeled Heat Flow From Constant Thermal Conductivities

Figure 10 shows a comparison between heat flow estimated from our Curie depth model (assuming constant thermal conductivity) and heat flow point measurements from the most recent compilation of Lucazeau (2019).

The estimated heat flow calculated from the global Curie depth model of Li et al. (2017) in southern Africa displays higher heat flow than our estimates for most study areas (cf. Figure S6 in the Supporting Information S1). In the Kapvaal Craton, e.g., the global model suggest an area of high values. The heat flow estimates based on our Curie depth model (with $\beta$ values of 2 and 2.5; Figures 10a and 10c) suggest a zone of moderate heat flow, in better agreement with the available measurements. This suggests that, in spite of the limitations of the method used to calculate the depth to the Curie isotherm, this method is useful in providing a lower thermal boundary condition for heat–flow calculations.

On the other hand, in areas with short-wavelength features–that significantly influence the heat flow field–heat flow cannot be estimated adequately. For instance, the Kalahari magnetic lineament at the western part of Kaapvaal Craton is modeled with very high heat flow values and shows large discrepancies to the measured low heat flow values, indicating that the estimated shallow Curie isotherm in this area might have a structural rather than a thermal origin.

### 5.2.2. Modeled Heat Flow From Varying Thermal Conductivities

Here, we consider heat flow models allowing for varying conductivities within the Bayesian framework described in Section 2.2.2 and Lösing et al. (2020). Figure S7 in the Supporting Information S1 indicates the correlations between the various involved quantities. The mantle heat flux $q_D$ correlates strongly with the LAB depth. A similar pattern can be observed for crustal heat production, which correlates with the Moho depth. In addition, there is a strong linear relation between heat production and heat flow, which has also been demonstrated empirically in Roy et al. (1968). The Curie depth shows correlation with heat production and heat flow. The heat flow ranges between 30 and 40 mW/m² in areas with greater Curie depths down to 40 km, with heat production below 1.0 $\mu$W/m². In regions with shallower Curie depths (between 15 and 20 km), the heat flow reaches up to 100 mW/m² and heat production takes higher rates up to 2.5 $\mu$W/m². The effect of the Moho depth and its uncertainty for the estimated heat flow is shown in Figure S8 in the Supporting Information S1. Generally, the modeled heat flow did not change significantly by changing the Moho depth within its uncertainty range of ±5 km.

Figure 11 eventually shows the two computed heat flow models (based on the Curie depth estimates for $\beta$ values of 2.0 and 2.5, respectively, and using a fixed Moho depth and LAB). In the Cape Fold Belt we observe areas of low heat flow, correlating with unrealistically estimated deep Curie depths. These particular regions are associated with high Curie depth uncertainties. In most places, the modeled heat flow in Figure 11 shows similar patterns as the modeled heat flow presented in Figure 10, although the latter used laterally constant heat production rates with a surface value of $H_0 = 2.5$ $\mu$W/m² and a constant thermal conductivity of 2.5 W/mK. This demonstrates the dominating effect of the Curie isotherm on heat flow calculations. However, along the Kalahari magnetic lineament, the results in Figure 11 for variable thermal conductivity show lower heat flow values than the results in Figure 10 for constant conductivity.

Both heat flow models (using laterally constant or variable heat production) show some degree of agreement compared to the measured heat flow values, however, with large discrepancies in most places. These can be explained by:

1. The shallow, spatially large magmatic provinces that run parallel to the Kalahari magnetic lineament can cause Curie depths to be underestimated.
2. Magmatic rocks with a large magnetic susceptibility may intrude and overlie a less magnetic metamorphic basement and sedimentary basin with an extremely weak magnetic field.
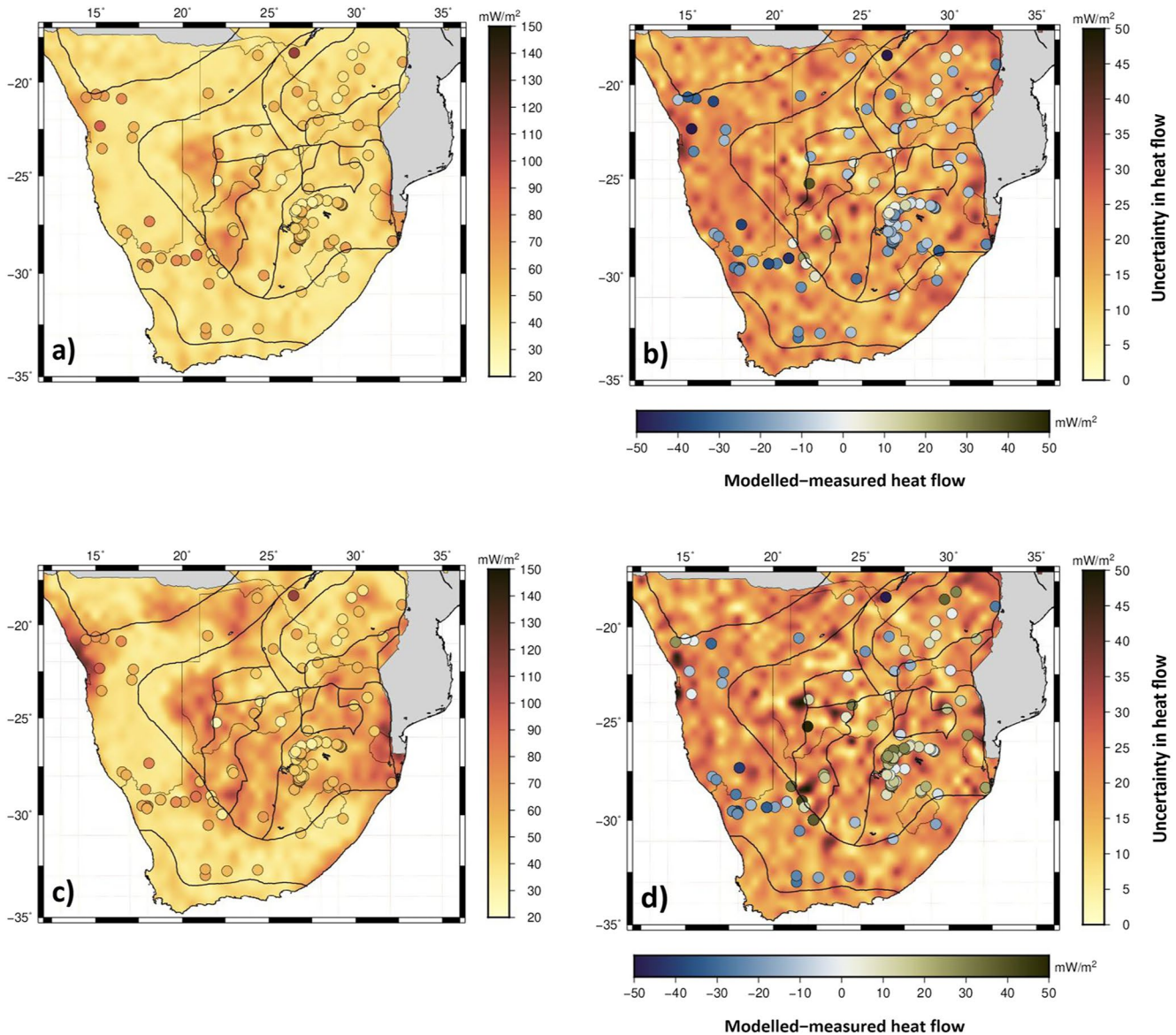
**Figure 11.** Modeled heat flow and its uncertainty when allowing laterally varying conductivities. Based on the estimated Curie depths when $\beta = 2.0$ (a) and $\beta = 2.5$ (c), overlain with the locations of measured heat flow data. Uncertainties of the modeled heat flow for the estimated Curie depth when $\beta = 2.0$ (b) and $\beta = 2.5$ (d), overlain with the difference between modeled and measured heat flow.

3. Shallow Curie depth and relatively low surface heat flow suggest a compositional rather than thermal control of the upper mantle, as suggested by seismic tomography and magnetotelluric results (Jones, 2017).

### 5.3. Comparison of Crustal Thickness With Curie Depths

As a result of high temperature, the mantle has been regarded as being nonmagnetic in most earlier studies (e.g., Wasilewski & Mayhew, 1992; Wasilewski et al., 1979). Ferré et al. (2014) and Blakely et al. (2005), however, argue that in certain geological contexts the upper mantle can be magnetized. In this study, we assumed that the Curie depth should not be significantly larger than the crustal thickness. Consequently, we define a maximum Curie depth of 50 km for our computations.
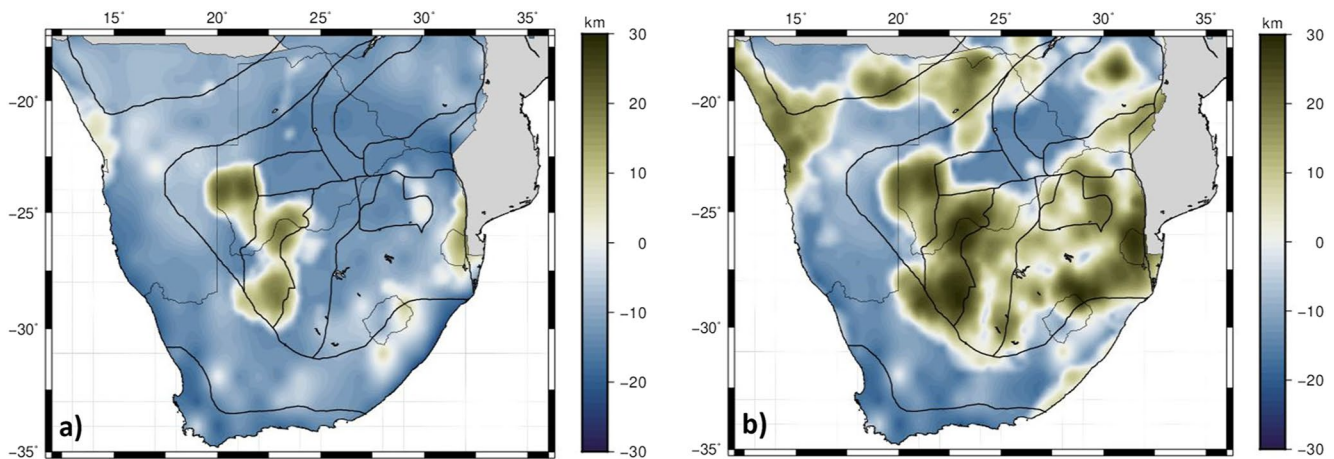
**Figure 12.** Comparison between Curie depth and the gravity inverted depth to Moho, (a) with $\beta = 2.0$ and (b) with $\beta = 2.5$. Curie depth values located below the Moho depth are represented by negative values, whereas Curie depth values above the Moho are represented by positive values.

A comparison between the crustal thickness and Curie depth is presented in Figure 12. Curie depths located below the Moho depths are represented by negative values, whereas Curie depths above the Moho are represented by positive values. Figure 12a shows that the bottom of the magnetic layer extends deeper than the Moho discontinuity in large areas, reaching the upper mantle and indicating that the Curie depth results with $\beta = 2.0$ may not be preferred. Figure 12b ($\beta = 2.5$) shows that although in large areas the estimated Curie depth is shallower than the Moho depth, along the Namaqua-Natal belt and Cape Fold belt it is deeper than Moho. That implies the upper mantle along these domains should be magnetized. If one does not want to rule this out as erroneous, it could be argued that this is due to high mafic content in the lower crust (Youssof et al., 2013). However, the areas of high uncertainties in our Curie depth estimates coincide with areas where the Curie depth is deeper than the depth to Moho (cf. Figure 5b).

## 6. Conclusions

In this study we first estimate Curie depth variations over southern Africa using a wavelet transform of magnetic anomaly data in combination with a Bayesian formalism. The sedimentary layer thickness used to constrain $z_t$ is kept constant for the inversion and different fractal parameters $\beta$ have been tested. The uncertainty in Curie depth estimation is provided along the entire study area, using a Bayesian approach. We observe correlations of shallow $z_b$ with the distribution of magmatic rocks at the western boundary of the Kaapvaal Craton, which is consistent among different $\beta$ values, indicating that the estimated $z_b$ is possibly more compositional dependant rather than thermally controlled. In general, Curie depth estimates from spectral analysis of magnetic anomaly data seem more reliable for young and hot tectonic domains.

In a second step, we use the estimated Curie depth to model surface heat flow, in a setup assuming either a constant thermal conductivity or varying thermal conductivities. The modeled heat flow matches the sparsely available heat flow data to a reasonable extent, except in regions where magmatic intrusions are present. The low heat flow along the Kaapvaal Craton further strengthens the interpretation that the estimated Curie depth is not only thermally controlled but also compositional dependent.

A final supporting observation for the latter statement comes from the comparison to a Moho depth model. Our obtained Curie depth estimates reveal large regions where the Curie depth is above the Moho but also large regions where it is below the Moho. However, this fact should not be overinterpreted since the regions with the deepest Curie depths are also those with the highest uncertainty.

It is to say that heat flow models based on Curie depth estimates remain the best assumption when no further information is available, in particular, in areas where heat flow data are very sparsely distributed. Future improvements on Curie depth estimates could be expected when jointly using magnetic anomaly data and the sparsely available heat flow measurements during the inversion process to obtain $z_b$.

## Data Availability Statement

All grid files and maps were created using Generic Mapping Tools (GMT) version 5 (Wessel et al., 2013). The scientific color map used in this study is available at (Crameri et al., 2020). The aeromagnetic data is available at (http://wdmam.org/) (Lesur et al., 2016). The sediment thickness model is available at (http://igppweb.ucsd.edu/~gabi/crust1.htm) (Laske et al., 2013). The heat flow data are available at (http://www.heatflow.org/) (Lucazeau, 2019). The wavelet analysis and Curie depth estimation were performed using the open-source software PlateCurie, freely available at (https://github.com/paudetseis/PlateCurie) (Audet & Gosselin, 2019). The resulting Curie depth and it is uncertainties and the modeled heat flow can be found at (https://doi.org/10.5281/zenodo.5070470). All the used data and the modeling software are cited within the manuscript and listed in the references.

## References

Afonso, J. C., Fullea, J., Griffin, W., Yang, Y., Jones, A. G., Connolly, J. A., & O'Reilly, S. Y. (2013). 3-d multiobservable probabilistic inversion for the compositional and thermal structure of the lithosphere and upper mantle. I: A priori petrological information and geophysical observables. *Journal of Geophysical Research: Solid Earth*, *118*(5), 2586–2617. https://doi.org/10.1002/jgrb.50124

Afonso, J. C., Salajegheh, F., Szwillus, W., Ebbing, J., & Gaina, C. (2019). A global reference model of the lithosphere and upper mantle from joint inversion and analysis of multiple data sets. *Geophysical Journal International*, *217*(3), 1602–1628. https://doi.org/10.1093/gji/ggz094

Amante, C. & Eakins, B. W. (2009). Etopo1 arc-minute global relief model: Procedures, data sources and analysis.

Andrés, J., Marzán, I., Ayarza, P., Martí, D., Palomeras, I., Torné, M., et al. (2018). Curie point depth of the Iberian Peninsula and surrounding margins. A thermal and tectonic perspective of its evolution. *Journal of Geophysical Research: Solid Earth*, *123*(3), 2049–2068. https://doi.org/10.1002/2017jb014994

Audet, P. (2020). PlateCurie: Software for mapping Curie depth from a wavelet analysis of magnetic anomaly data (v0.0.1). *Zenodo*. https://doi.org/10.5281/zenodo.3905424

Audet, P., & Gosselin, J. M. (2019). Curie depth estimation from magnetic anomaly data: A re-assessment using multitaper spectral analysis and Bayesian inference. *Geophysical Journal International*, *218*(1), 494–507. https://doi.org/10.1093/gji/ggz166

Begg, G., Griffin, W., Natapov, L., O'Reilly, S. Y., Grand, S., O'Neill, C., et al. (2009). The lithospheric architecture of Africa: Seismic tomography, mantle petrology, and tectonic evolution. *Geosphere*, *5*(1), 23–50. https://doi.org/10.1130/ges00179.1

Blakely, R. J. (1988). Curie temperature isotherm analysis and tectonic implications of aeromagnetic data from Nevada. *Journal of Geophysical Research*, *93*(B10), 11817–11832. https://doi.org/10.1029/jb093ib10p11817

Blakely, R. J., Brocher, T. M., & Wells, R. E. (2005). Subduction-zone magnetic anomalies and implications for hydrated forearc mantle. *Geology*, *33*(6), 445–448. https://doi.org/10.1130/g21447.1

Bouligand, C., Glen, J. M. G., & Blakely, R. J. (2009). Mapping Curie temperature depth in the western United States with a fractal model for crustal magnetization. *Journal of Geophysical Research*, *114*(B11), B11104. https://doi.org/10.1029/2009JB006494

Campbell, I., Naldrett, A., & Barnes, S. (1983). A model for the origin of the platinum-rich sulfide horizons in the bushveld and stillwater complexes. *Journal of Petrology*, *24*(2), 133–165. https://doi.org/10.1093/petrology/24.2.133

Catalán, M., Dyment, J., Choi, Y., Hamoudi, M., Lesur, V., Thébault, E., et al. (2016). Making a better magnetic map. *EOS*.

Celli, N. L., Lebedev, S., Schaeffer, A. J., & Gaina, C. (2020). African cratonic lithosphere carved by mantle plumes. *Nature Communications*, *11*(1), 1–10. https://doi.org/10.1038/s41467-019-13871-2

Chopping, R., & Kennett, B. L. (2013). The curie depth of Australia, and its uncertainty. *ASEG Extended Abstracts*, *2013*(1), 1–3. https://doi.org/10.1071/aseg2013ab199

Cornell, D. H., Van Schijndel, V., Ingolfsson, O., Scherstén, A., Karlsson, L., Wojtyla, J., & Karlsson, K. (2011). Evidence from Dwyka tillite cobbles of Archaean basement beneath the Kalahari sands of southern Africa. *Lithos*, *125*(1–2), 482–502. https://doi.org/10.1016/j.lithos.2011.03.006

Crameri, F., Shephard, G. E., & Heron, P. J. (2020). The misuse of colour in science communication. *Nature Communications*, *11*(1), 1–10. https://doi.org/10.1038/s41467-020-19160-7

de Wit, M. J., Jones, M. G., & Buchanan, D. L. (1992). The geology and tectonic evolution of the Pietersburg greenstone belt, south Africa. *Precambrian Research*, *55*(1–4), 123–153. https://doi.org/10.1016/0301-9268(92)90019-k

Duncan, R. A., Hooper, P., Rehacek, J., Marsh, J., & Duncan, A. (1997). The timing and duration of the Karoo igneous event, southern Gondwana. *Journal of Geophysical Research*, *102*(B8), 18127–18138. https://doi.org/10.1029/97jb00972

Dunlop, D. J., & Özdemir, Ö. (2001). *Rock magnetism: Fundamentals and frontiers (No. 3)*. Cambridge University Press.

Ebbing, J., Gernigon, L., Pascal, C., Olesen, O., & Osmundsen, P. T. (2009). A discussion of structural and thermal control of magnetic anomalies on the mid-Norwegian margin. *Geophysical Prospecting*, *57*(4), 665–681. https://doi.org/10.1111/j.1365-2478.2009.00800.x

Ebbing, J., Szwillus, W., & Dilixiati, Y. (2021). *A Bayesian framework for simultaneous determination of susceptibility and magnetic thickness from magnetic data (Tech. Rep.)*.

Ellwood, B. B., Crick, R. E., Hassani, A. E., Benoist, S. L., & Young, R. H. (2000). Magnetosusceptibility event and cyclostratigraphy method applied to marine rocks: Detrital input versus carbonate productivity. *Geology*, *28*(12), 1135–1138. https://doi.org/10.1130/0091-7613(2000)028<1135:meacma>2.3.co;2

Ernst, R. E., Pereira, E., Hamilton, M. A., Pisarevsky, S. A., Rodriques, J., Tassinari, C. C., et al. (2013). Mesoproterozoic intraplate magmatic 'barcode' record of the Angola portion of the Congo Craton: Newly dated magmatic events at 1505 and 1110 ma and implications for Nuna (Columbia) supercontinent reconstructions. *Precambrian Research*, *230*, 103–118. https://doi.org/10.1016/j.precamres.2013.01.010

Fadel, I., Paulssen, H., van der Meijde, M., Kwadiba, M., Ntibinyane, O., Nyblade, A., & Durrheim, R. (2020). Crustal and upper mantle shear wave velocity structure of Botswana: The 3 April 2017 central Botswana earthquake linked to the east African rift system. *Geophysical Research Letters*, *47*(4), e2019GL085598. https://doi.org/10.1029/2019gl085598

Fadel, I., van der Meijde, M., & Paulssen, H. (2018). Crustal structure and dynamics of Botswana. *Journal of Geophysical Research: Solid Earth*, *123*(12), 10–659. https://doi.org/10.1029/2018jb016190

Ferré, E. C., Friedman, S. A., Martín-Hernández, F., Feinberg, J. M., Till, J. L., Ionov, D. A., & Conder, J. A. (2014). Eight good reasons why the uppermost mantle could be magnetic. *Tectonophysics*, *624–625*, 3–14. https://doi.org/10.1016/j.tecto.2014.01.004

Gard, M., & Hasterok, D. (2021). A global curie depth model utilising the equivalent source magnetic dipole method. *Physics of the Earth and Planetary Interiors*, *313*, 106672. https://doi.org/10.1016/j.pepi.2021.106672

Gaudreau, E., Audet, P., & Schneider, D. (2019). Mapping curie depth across western Canada from a wavelet analysis of magnetic anomaly data. *Journal of Geophysical Research: Solid Earth*, *124*(5), 4365–4385. https://doi.org/10.1029/2018JB016726

Goodwin, A. (1996). *Principles of Precambrian geology*. Academic Press.

Haggerty, S. E. (1978). Mineralogical constraints on Curie isotherms in deep crustal magnetic anomalies. *Geophysical Research Letters*, *5*(2), 105–108. https://doi.org/10.1029/gl005i002p00105

Hanson, R. (2003). Proterozoic geochronology and tectonic evolution of southern Africa. *Geological Society, London, Special Publications*, *206*(1), 427–463. https://doi.org/10.1144/gsl.sp.2003.206.01.20

Hanson, R. E., Crowley, J. L., Bowring, S. A., Ramezani, J., Gose, W. A., Dalziel, I. W. D., et al. (2004). Coeval large-scale magmatism in the Kalahari and Laurentian cratons during Rodina Assembly. *Science*, *304*(5674), 1126–1129. https://doi.org/10.1126/science.1096329

Hasterok, D., & Chapman, D. (2011). Heat production and geotherms for the continental lithosphere. *Earth and Planetary Science Letters*, *307*(1–2), 59–70. https://doi.org/10.1016/j.epsl.2011.04.034

Hutchins, D., & Reeves, C. (1980). Regional geophysical exploration of the Kalahari in Botswana. *Tectonophysics*, *69*(3), 201–220. https://doi.org/10.1016/0040-1951(80)90211-5

Jelsma, H. A., & Dirks, P. H. (2002). Neoarchaean tectonic evolution of the Zimbabwe craton. *Geological Society, London, Special Publications*, *199*(1), 183–211. https://doi.org/10.1144/gsl.sp.2002.199.01.10

Johnson, M., Van Vuuren, C., Visser, J., Cole, D., Wickens, H. D. V., Christie, A., & Roberts, D. (1997). The foreland Karoo basin, South Africa. In *Sedimentary basins of the world* (Vol. *3*, pp. 269–317). Elsevier. https://doi.org/10.1016/s1874-5997(97)80015-9

Jones, M. (2017). Heat flow in the Bushveld Complex, South Africa: Implications for upper mantle structure. *South African Journal of Geology*, *120*(3), 351–370. https://doi.org/10.25131/gssajg.120.3.351

Kaban, M. K., Tesauro, M., Mooney, W. D., & Cloetingh, S. A. P. L. (2014). Density, temperature, and composition of the North American lithosphere—New insights from a joint analysis of seismic, gravity, and mineral physics data: 1. Density structure of the crust and upper mantle. *Geochemistry, Geophysics, Geosystems*, *15*(12), 4781–4807. https://doi.org/10.1002/2014GC005483

Key, R. M., & Ayres, N. (2000). The 1998 edition of the national geological map of Botswana. *Journal of African Earth Sciences*, *30*(3), 427–451. https://doi.org/10.1016/s0899-5362(00)00030-0

Kirby, J. F. (2005). Which wavelet best reproduces the Fourier power spectrum? *Computers & Geosciences*, *31*(7), 846–864. https://doi.org/10.1016/j.cageo.2005.01.014

Lachenbruch, A. H. (1970). Crustal temperature and heat production: Implications of the linear heat-flow relation. *Journal of Geophysical Research*, *75*(17), 3291–3300. https://doi.org/10.1029/jb075i017p03291

Laske, G., Masters, G., Ma, Z., & Pasyanos, M. (2013). Update on CRUST1. 0–A 1-degree global model of Earth's crust. *Geophysical Research Abstracts*, *15*, 2658.

Leseane, K., Atekwana, E. A., Mickus, K. L., Abdelsalam, M. G., Shemang, E. M., & Atekwana, E. A. (2015). Thermal perturbations beneath the incipient Okavango rift zone, northwest Botswana. *Journal of Geophysical Research: Solid Earth*, *120*(2), 1210–1228. https://doi.org/10.1002/2014jb011029

Lesur, V., Hamoudi, M., Choi, Y., Dyment, J., & Thébault, E. (2016). Building the second version of the world digital magnetic anomaly map (WDMAM). *Earth Planets and Space*, *68*(1), 1–13. https://doi.org/10.1186/s40623-016-0404-6

Li, C., Lu, Y., & Wang, J. (2017). A global reference model of curie-point depths based on EMAG2. *Scientific Reports*, *7*, 45129. https://doi.org/10.1038/srep45129

Lösing, M., Ebbing, J., & Szwillus, W. (2020). Geothermal heat flux in Antarctica: Assessing models and observations by Bayesian inversion. *Frontiers of Earth Science*, *8*, 105. https://doi.org/10.3389/feart.2020.00105

Lucazeau, F. (2019). Analysis and mapping of an updated terrestrial heat flow data set. *Geochemistry, Geophysics, Geosystems*, *20*(8), 4001–4024. https://doi.org/10.1029/2019GC008389

Martos, Y. M., Catalán, M., Jordan, T. A., Golynsky, A., Golynsky, D., Eagles, G., & Vaughan, D. G. (2017). Heat flux distribution of Antarctica unveiled. *Geophysical Research Letters*, *44*(2211), 11417–11426. https://doi.org/10.1002/2017GL075609

Mather, B., & Delhaye, R. (2019). PyCurious: A python module for computing the curie depth from the magnetic anomaly. *Journal of Open Source Software*, *4*(39), 1544. https://doi.org/10.21105/joss.01544

Mather, B., & Fullea, J. (2019). Constraining the geotherm beneath the British Isles from Bayesian inversion of Curie depth: Integrated modelling of magnetic, geothermal, and seismic data. *Solid Earth*, *10*(3), 839–850. https://doi.org/10.5194/se-10-839-2019

Maus, S., Gordon, D., & Fairhead, D. (1997). Curie-temperature depth estimation using a self-similar magnetization model. *Geophysical Journal International*, *129*(1), 163–168. https://doi.org/10.1111/j.1365-246X.1997.tb00945.x

McCourt, S., Hilliard, P., Armstrong, R., & Munyanyiwa, H. (2001). SHRIMP U-Pb zircon geochronology of the Hurungwe granite northwest Zimbabwe: Age constraints on the timing of the Magondi orogeny and implications for the correlation between the Kheis and Magondi belts. *South African Journal of Geology*, *104*(1), 39–46. https://doi.org/10.2113/104.1.39

Núñez, D., Prezzi, C., & Sánchez Bettucci, L. (2021). Review of Curie point depth determination through different spectral methods applied to magnetic data. *Geophysical Journal International*, *224*(1), 17–39. https://doi.org/10.1002/2013EO450001

Olsen, N., Ravat, D., Finlay, C. C., & Kother, L. K. (2017). LCS-1: A high-resolution global model of the lithospheric magnetic field derived from CHAMP and Swarm satellite observations. *Geophysical Journal International*, *211*(3), 1461–1477. https://doi.org/10.1093/gji/ggx381

Olsson, J., Söderlund, U., Klausen, M., & Ernst, R. (2010). U–Pb baddeleyite ages linking major Archean dyke swarms to volcanic-rift forming events in the Kaapvaal craton (South Africa), and a precise age for the bushveld complex. *Precambrian Research*, *183*(3), 490–500. https://doi.org/10.1016/j.precamres.2010.07.009

Pollack, H. N., Hurter, S. J., & Johnson, J. R. (1993). Heat flow from the Earth's interior: Analysis of the global data set. *Reviews of Geophysics*, *31*(3), 267–280. https://doi.org/10.1029/93rg01249

Reeves, C. (1978). *Reconnaissance aeromagnetic survey of Botswana 1975–77: Final interpretation report:*. Geological Survey Department.

Riley, T., Curtis, M., Leat, P., Watkeys, M., Duncan, R., Millar, I., & Owens, W. (2006). Overlap of Karoo and Ferrar magma types in Kwazulu-Natal, South Africa. *Journal of Petrology*, *47*(3), 541–566. https://doi.org/10.1093/petrology/egi085

Roy, R. F., Blackwell, D. D., & Birch, F. (1968). Heat generation of plutonic rocks and continental heat flow provinces. *Earth and Planetary Science Letters*, *5*, 1–12. https://doi.org/10.1016/S0012-821X(68)80002-0

Salem, A., Green, C., Ravat, D., Singh, K. H., East, P., Fairhead, J. D., et al. (2014). Depth to Curie temperature across the central red sea from magnetic data using the de-fractal method. *Tectonophysics*, *624*, 75–86. https://doi.org/10.1016/j.tecto.2014.04.027

Scheiber-Enslin, S., Ebbing, J., & Webb, S. J. (2014). An integrated geophysical study of the beattie magnetic anomaly, South Africa. *Tectonophysics*, *636*, 228–243. https://doi.org/10.1016/j.tecto.2014.08.021

Schmitz, M., & Bowring, S. (2003). Ultrahigh-temperature metamorphism in the lower crust during Neoarchean Ventersdorp rifting and magmatism, Kaapvaal Craton, Southern Africa. *Geological Society of America Bulletin*, *115*, 533–548. https://doi.org/10.1130/0016-7606(2003)115<0533:umitlc>2.0.co;2

Sobh, M., Ebbing, J., Mansi, A. H., & Götze, H.-J. (2019). Inverse and 3D forward gravity modelling for the estimation of the crustal thickness of Egypt. *Tectonophysics*, *752*, 52–67. https://doi.org/10.1016/j.tecto.2018.12.002

Sobh, M., Ebbing, J., Mansi, A. H., Götze, H.-J., Emry, E., & Abdelsalam, M. (2020). The lithospheric structure of the Saharan metacraton from 3-D integrated geophysical-petrological modeling. *Journal of Geophysical Research: Solid Earth*, *125*(8), e2019JB018747. https://doi.org/10.1029/2019jb018747

Stettler, E., Fourie, C., & Cole, P. (2000). *Total magnetic field intensity map of the republic of South Africa*. Council for Geoscience.

Tanaka, A., Okubo, Y., & Matsubayashi, O. (1999). Curie point depth based on spectrum analysis of the magnetic anomaly data in east and Southeast Asia. *Tectonophysics*, *306*(3–4), 461–470. https://doi.org/10.1016/s0040-1951(99)00072-4

Thomas, R., Von Veh, M., & McCourt, S. (1993). The tectonic evolution of southern Africa: An overview. *Journal of African Earth Sciences*, *16*(1–2), 5–24. https://doi.org/10.1016/0899-5362(93)90159-n

Uieda, L., & Barbosa, V. C. F. (2017). Fast nonlinear gravity inversion in spherical coordinates with application to the South American Moho. *Geophysical Journal International*, *208*(1), 162–176. https://doi.org/10.1093/gji/ggw390

Van Schijndel, V., Cornell, D. H., Hoffmann, K.-H., & Frei, D. (2011). Three episodes of crustal development in the Rehoboth province, Namibia. *Geological Society, London, Special Publications*, *357*(1), 27–47. https://doi.org/10.1144/sp357.3

Wasilewski, P. J., & Mayhew, M. A. (1992). The Moho as a magnetic boundary revisited. *Geophysical Research Letters*, *19*(22), 2259–2262. https://doi.org/10.1029/92GL01997

Wasilewski, P. J., Thomas, H. H., & Mayhew, M. A. (1979). The Moho as a magnetic boundary. *Geophysical Research Letters*, *6*(7), 541–544. https://doi.org/10.1029/GL006i007p00541

Weckmann, U., Ritter, O., Jung, A., Branch, T., & De Wit, M. (2007). Magnetotelluric measurements across the Beattie magnetic anomaly and the Southern Cape Conductive Belt, South Africa. *Journal of Geophysical Research*, *112*(B5), B05416. https://doi.org/10.1029/2005jb003975

Wessel, P., Smith, W. H. F., Scharroo, R., Luis, J., & Wobbe, F. (2013). Generic mapping tools: Improved version released. *EOS, Transactions American Geophysical Union*, *94*(45), 409–410. https://doi.org/10.1002/2013EO450001

White-Gaynor, A. L., Nyblade, A. A., Durrheim, R., Raveloson, R., van der Meijde, M., Fadel, I., et al. (2020). Lithospheric boundaries and upper mantle structure beneath southern Africa imaged by *P* and *S* wave velocity models. *Geochemistry, Geophysics, Geosystems*, *21*(10), e2020GC008925. https://doi.org/10.1029/2020GC008925

Wright, J. A., & Hall, J. (1990). Deep seismic profiling in the Nosop Basin, Botswana: Cratons, mobile belts and sedimentary basins. *Tectonophysics*, *173*(1–4), 333–343. https://doi.org/10.1016/0040-1951(90)90228-z

Youssof, M., Thybo, H., Artemieva, I., & Levander, A. (2013). Moho depth and crustal composition in southern Africa. *Tectonophysics*, *609*, 267–287. https://doi.org/10.1016/j.tecto.2013.09.001